UNIVERSIDAD NACIONAL AUTÓNOMA DE MÉXICO
PROGRAMA DE POSGRADO EN INGENIERÍA
INSTITUTO DE ENERGÍAS RENOVABLES
ÁREA SISTEMAS ENERGÉTICOS

ELECTROMAGNETIC STIRRING AT MILLIMETRIC SCALE

TESIS
QUE PARA OPTAR POR EL GRADO DE
MAESTRO EN INGENIERÍA EN ENERGÍA

PRESENTA:

JOSE MANUEL OLVERA OROZCO

DIRECTORES DE TESIS:

DR. ALDO FIGUEROA LARA
CONACYT–CENTRO DE INVESTIGACIÓN EN CIENCIAS–UAEM

DR. SERGIO CUEVAS GARCÍA
INSTITUTO DE ENERGÍAS RENOVABLES–UNAM

TEMIXCO, MORELOS – SEPTIEMBRE 2020

Electromagnetic stirring at millimetric scale

Tutors: Dr. Aldo Figueroa Lara[1] & Dr. Sergio Cuevas García[2]

[1]Conacyt–Centro de Investigación en Ciencias, Universidad Autónoma del Estado de Morelos
[2]Instituto de Energías Renovables, Universidad Nacional Autónoma de México

Master's Thesis

Jose Manuel Olvera Orozco

Instituto de Energías Renovables
Universidad Nacional Autónoma de México
July, 2020

ELECTROMAGNETIC STIRRING AT MILLIMETRIC SCALE

JOSE MANUEL OLVERA OROZCO

Instituto de Energías Renovables
UNAM

Abstract

An experimental and theoretical study of electromagnetically driven laminar vortical flows at a millimetric scale in a shallow layer of electrolyte is presented. The force that sets the electrolyte in motion is the Lorentz force, which is generated by the interaction of applied direct electric currents and the magnetic field distribution due to one and several dipolar permanent magnets. The flow is analyzed inside a region of approximately 10 mm × 10 mm. Velocity fields are obtained at the free surface using particle image velocimetry in a planar configuration parallel to the bottom wall. Streamlines are obtained experimentally by tracking particles at the free surface through long exposure photographs. The experimental results are qualitatively compared with a two dimensional (2D) numerical simulation which for simplicity ignores the friction from the bottom wall in the small depth (1 mm) electrolyte layer, and to an analytical solution derived from an asymptotic expansion that uses a point dipole expression to replicate the magnetic field distribution. The numerical simulation uses an analytical expression to replicate the non–uniformity of the experimental magnetic field distribution, resulting in accurate comparisons. The aspect ratio of the horizontal extent of the electrolyte layer to its vertical depth is large, which justifies the 2D model and allows for a reasonable approach. On the other hand, the point dipole expression limits the capacity of the analytical solution to completely replicate vortex interactions. However, it is able to capture the main characteristics of the experimental results such as the distribution of the vortices with respect to the magnetic field source. The numerical results show a good qualitative agreement with the experimental observations.

Vorticity fields are obtained, which reveal strong velocity gradients over millimetric length scales. The electromagnetic interactions owing to complicated magnetic field distributions produce symmetrically intriguing and interesting flow patterns whose dynamics cannot be easily anticipated. Contrarily, simpler structured magnetic field distributions generate symmetrical flow patterns whose flow field can be quickly predicted. Owing to the weak strength of the Lorentz force and to the millimetric confinement of the shallow electrolyte layer, the time–independent laminar flow under study is characterized by a small Reynolds number.

Resumen

Se presenta un estudio experimental y teórico de flujos de vórtices forzados electromagnéticamente en una escala milimétrica en una capa delgada de electrolito. La fuerza que genera movimiento en el electrolito es la fuerza de Lorentz, la cual es generada por la interacción de corriente directa impuesta, con la distribución del campo magnético debido a uno y varios imanes dipolares permanentes. El flujo es analizado dentro de una región de 10 mm × 10 mm aproximadamente. Se obtienen campos de velocidad en la superficie libre utilizando velocimetría de imágenes por partículas en una configuración cuyo plano es paralelo a la pared del fondo. Se obtienen líneas de corriente experimentalmente mediante el trazado de partículas en la superificie libre utilizando fotografía de larga exposición. Los resultados experimentales se comparan cualitativamente con una simulación numérica bidimensional (2D), que por simplicidad ignora la fricción de la pared del fondo en la capa de electrolito de baja profundidad (1 mm). También se comparan con una solución analítica derivada de una expansión asintótica que utiliza una expresión de dipolo puntual para replicar la distribución del campo magnético. La simulación numérica utiliza una expresión analítica para replicar la distribución no–uniforme del campo magnético experimental, lo cual resulta en comparaciones precisas. La razón de aspecto es grande respecto a la dimensión horizontal de la capa de electrolito sobre la profundidad vertical, lo que justifica el modelo 2D y da lugar a una aproximación razonable. Por otro lado, la capacidad de la solución analítica para replicar completamente la interacción de los vórtices se ve limitada por la expresión del dipolo puntual. Aun así, logra capturar las características principales de los resultados experimentales, tal como la distribución de los vórtices con respecto al origen del campo magnético. Los resultados numéricos demuestran una comparación cualitativamente aceptable con las observaciones experimentales.

Se obtienen campos de vorticidad donde se revelan fuertes gradientes de velocidad a lo largo de distancias milimétricas. Las interacciones electromagnéticas producidas por distribuciones complicadas de campo magnético, generan patrones de flujos simétricos intrigantes, e interesantes cuya dinámica no puede ser fácilmente anticipada. Por el contrario, distribuciones de campo magnético más simples, generan patrones de flujos simétricos cuyo campo de flujo puede ser rápidamente predicho. Debido a la intensidad débil de la fuerza de Lorentz y al confinamiento milimétrico de la capa delgada de electrolito, el flujo independiente del tiempo bajo estudio se caracteriza por un número bajo de Reynolds.

Contents

Chapter 1

Introduction

Magnetohydrodynamics (MHD) is the field of physics and engineering that studies the coupling between fluid dynamics and electromagnetism. The coupling of these two concepts describes the interaction of electrically conducting (non–magnetizable) fluids and magnetic fields, where the fluids concerned can be plasmas, liquid metals, or electrolytes.

In geophysical and astrophysical phenomena a magnetic field arises naturally, as occurs in Earth's molten core which originates what is known as the geodynamo. The dynamo theory of the earth argues that convective and buoyancy motions in the liquid core induce electrical currents that consequently create an induced magnetic field. In the solar context, on the other hand, sunspots and solar flares are a manifestation of the solar magnetic field.

Artificial magnetic fields generated by means of an electromagnet or a permanent magnet find a wide spectrum of applications for the use of conducting fluids in laboratory and industry. Industrial applications of MHD include, for instance, the heating, stirring, mixing, and pumping of conducting liquids, among other processes. Common practices in metallurgy involve the use of magnetic fields to transport molten metal through conveyor belts; the use of induced currents for magnetic damping of jets and vortices; and the use of rotating magnetic fields to homogenize casts, with the ultimate goal of getting high quality products of fine grain and very little or no porosity at all. In nuclear fusion, MHD has a prominent role in plasma confinement using superconducting magnets, as well as in the heat extraction based in liquid metal blankets (Bühler 2007). The chemical industry uses MHD for electrochemical processing of materials and to study transport phenomena of chemical species. The field of microfluidics has also benefited in the past decades by several MHD applications (Qian *et al.* 2002), some of which have been of interest to the biomedical community such as actuation devices, micromixers and sensors (Stanley *et al.* 2016). These are particularly useful in applications suited for Lab–On–A–Chip (LOC) technology, which requires the least amount of working parts for highly specialized processes such as cell sorting and point–of–care diagnostics (Khoshmanesh *et al.* 2017).

Electromagnetic forces have been extensively used to generate vorticity, which is fundamental in many transport processes over a wide range of scales, and can take place in natural phenomena and technological applications. The generation of vorticity is diverse, it can be due to natural agents such as the wind, marine currents, or Earth's rotation. On the other hand, artificially generated vorticity with different mechanisms is common in several industrial applications. On the geophysical scale, where most events are related to a turbulent regime, ocean vortices, which are a fundamental ingredient for the continuity of life, are found dispersed throughout the world. These vortices can develop radiuses on the hundreds of kilometers and can last for days, months or even years. Among their vital functions, one of their main purposes is to transport heat throughout Earth's oceans. They also distribute salt, nutrients, chemicals and other biological substances and, to some degree, determine our climate and sustain worldwide ocean circulation (Thompson & Robb McDonald 1999). However, vortices can be troublesome at times. This is the case of tornadoes and hurricanes which can have disastrous consequences while their full

understanding is still an open scientific challenge. On the other hand, airplanes produce long–lived wake vortices at take off and landing. These trailing wakes span for hundreds of meters and are dangerous for airplanes behind them. This means pilots have to distance themselves substantially in order to avoid the turbulence and destabilization, which in turn hinders the growth of air traffic (Schöll *et al.* 2010). On a much smaller scale, at a creeping flow regime that is frequently related to highly viscous flows, vortex formations are also common in the biological context. Rossen *et al.* (2014) reported experimental and numerical vorticity patterns, which were the result of long–range interactions in tissue flows owing to the process of endothelial cell division. Vortical structures are ubiquitous in nature and many present a high degree of complexity. In fact, looking at a coffee cup with a drop of milk while it is stirred will reveal how intricate vortices can be.

It is important to clarify that stirring and mixing are related operations but they are not the same. Stirring can be understood as an induced circulating motion of a fluid without diffusion. On the other hand, mixing is concerned with concentration gradients. According to Villermaux (2019), mixing is the operation by which a system evolves from the initial segregation of the constituents to their complete uniformity. Thus, mixing affects concentration homogeneity at a molecular scale. Although mixing can be reached without stirring, say a in a quiescent fluid, it is through stirring that a mixture can reach a higher level of homogeneity faster. Stirring can be handled in such a way that a *reversible* process can be achieved (see figure 1.1), whereas mixing is considered to be an irreversible phenomena (Villermaux 2019).
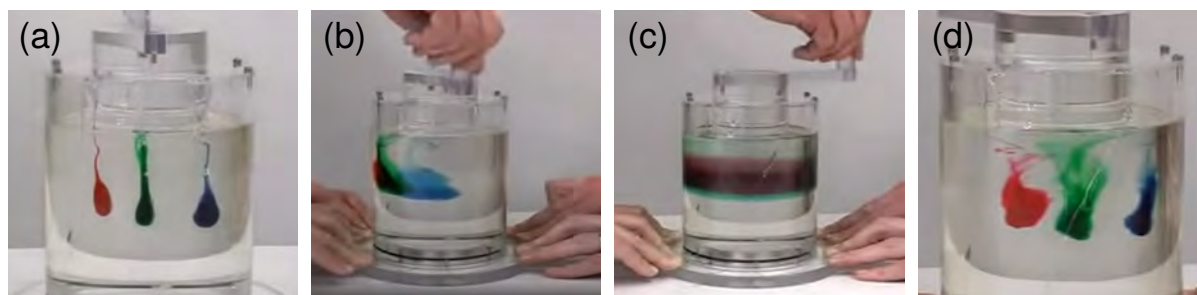

FIGURE 1.1: Laminar flow between axially concentric cylinders. In **(a)** the gap is filled with glycerol and the colored drops are colored tracers; **(b)** a very slow clockwise turning of the inner cylinder forms the drops into laminar layers; **(c)** the inner cylinder is cranked counterclockwise with the same amount of turns; **(d)** although slightly deformed, the drops recover their initial shape. The snapshots were taken from a YouTube video of the University of New Mexico's Physics and Astronomy Department: https://www.youtube.com/watch?v=p08_KlTKP50

Electromagnetic forces, originated from the interaction of electric currents and magnetic fields, can be efficiently used to generate motion in electrolytes and liquid metals. Owing to their non–intrusive nature, these rotational forces, usually known as Lorentz forces, are able to produce stirring and consequently to generate vorticity in electrically conducting fluids without mechanical parts in contact with the working fluid. Electromagnetic forcing has been used experimentally in shallow layers of liquid metal to produce mixing (Sommeria 1988). Stirring has been produced experimentally using eccentric cylinders with two pairs of circular electrodes under an axial magnetic field (Yi *et al.* 2002). More recently, electromagnetic forcing has been applied to shallow layers of electrolyte in two–layer configurations to study free surface flows and three–dimensional effects (Martell *et al.* 2019; Tithof *et al.* 2018).

In the present work, electromagnetic stirring is used to produce vorticity patterns in shallow electrolyte layers with very low Reynolds numbers using different magnet configurations in a cell with millimetric dimensions. Low Reynolds numbers are associated to laminar flows, for this reason, the electrolyte is forced in a small scale cell with characteristics that confine the flow to a narrow region, and the injected current is limited to an intensity that

is in accordance with the low Reynolds number character of the flow (see figure 1.2).
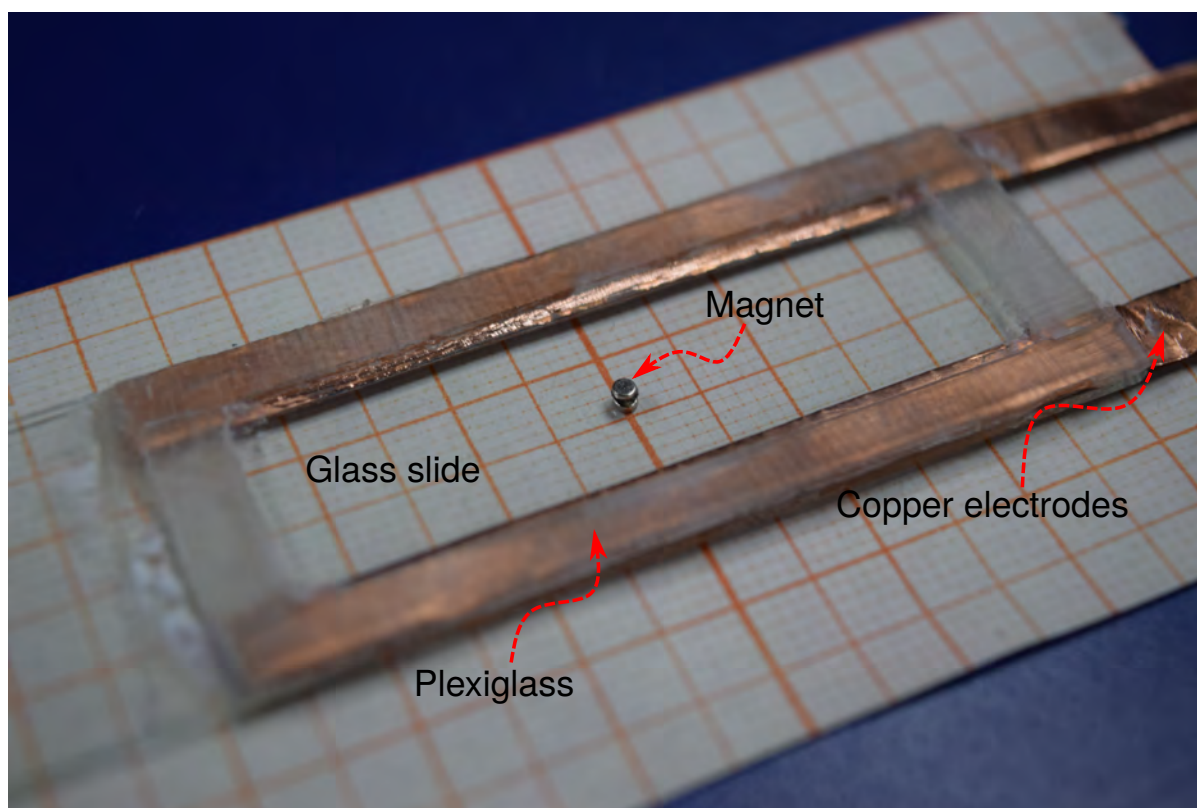

FIGURE 1.2: MHD cell. The millimetric–scale graph allows to visualize the size of the magnet and cell. In the actual experiment, the lower bottom of the glass slide was painted with a coat of mate black paint to enhance contrast.

A rectangular cell of 60×25 mm and 3 mm height made of glass was used with two copper electrodes 65 mm long placed in the longer side. The electrolyte is a mixture of water and sodium bicarbonate at 8.6% in weight. Permanent dipole magnets of 1.5 mm diameter made of a neodymium alloy were used. The magnets are axially polarized, thus their main component is on the vertical axis. The magnets are configured into geometrical shapes and positioned underneath. The uniform current is regulated using a DC constant voltage source and flows through the electrolyte from one electrode to the other. The visualizations are performed using topside illumination only with LED lamps, and the camera is positioned atop the cell. The flow is tracked using hollow glass spheres of ~ 10 µm diameter. The tracers are recorded using a digital camera and a lens with a focal length of 105 mm to get a naturally narrow field of view of the experiment. The experimental results are obtained using Particle Image Velocimetry and long exposure photography. Two main drawbacks of this configuration were the effect of electrolysis owing to the use of a DC source, and particle aggregation due to particle interactions at the free surface. However, as will be shown, the results were satisfactory. It is expected that in further experiments, the results can be compared quantitatively, and that the experiments can be realized using a constant current source.

The aim of this thesis is to explore electromagnetically driven low Reynolds number flows at millimetric scale and to qualitatively compare time–independent experimental flows with results from a numerical simulation and analytical solutions. While in the experiment a cylindrical magnet is used, the simulation makes use of an expression implemented for magnetized square surfaces, and the analytical solution uses an expression for a point

dipole magnet. The latter has certain limitations which lead to a coarse representation of the general flow. On the other hand, the experiment and the simulation deliver favorable results that are in very good qualitative agreement. One of the characteristics of the flows explored in the present work is the great symmetry in the vorticity patterns that are obtained (see figure 1.3).
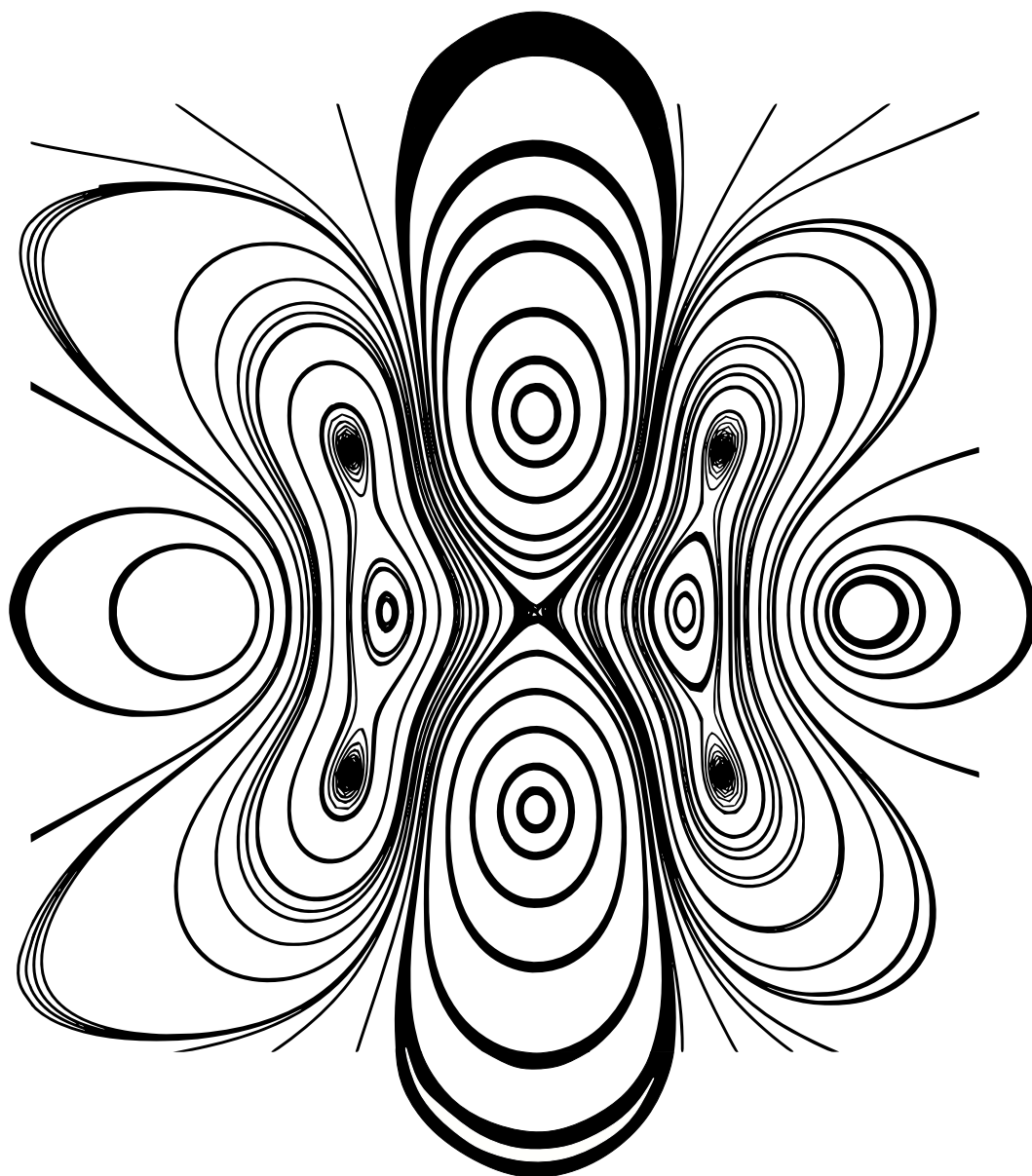
FIGURE 1.3: Streamlines generated by six magnets arranged in the shape of a hexagon.

Experimental velocity fields as well as velocity and vorticity maps were compared with numerical and analytical results. The velocity maps help to identify useful regions for a wide range of applications. In fact, the velocity fields give account of magnet misalignments which introduced asymmetry into the results, also appreciated in the velocity maps. In addition, interesting features can be observed through the study of vorticity maps. In our case,

the voltage is kept low so that temporal dependent flows can be discarded. As is expected, a single magnet produces a dipolar vortex; on the other hand, multiple magnets produce complicated dynamics but interesting flow patterns.

The work is structured as follows. In Chapter 2, the mathematical formulation of the thesis is described. The equations of viscous flow are coupled with the Lorentz force term to derive the system of equations used to describe the MHD flow. The non–dimensionalization and the main assumptions are also presented. In Chapter 3, the experimental procedures are detailed. Then, in Chapter 4 the analytical solutions to the MHD problem are obtained for the multiple magnet configurations. Finally, a purely two–dimensional numerical model is derived using a second order finite differences method. This model ignores the friction from bottom wall. The results are presented in Chapter 5 offering an explanation and highlighting some relevant experimental observations. As will be seen, the comparisons are satisfactory in qualitative terms. Finally, the conclusions and future work are shown in Chapter 6.

Chapter 2

Problem formulation

This chapter includes three sections in which the physical principles and the mathematical equations used to describe the physics of the experiments in this thesis are presented. The first section introduces the Navier-Stokes equation and the continuity equation which are used to describe the flow of viscous fluids. The second section presents the equations of MHD, emphasizing on the Lorentz force $\vec{F} = \vec{J} \times \vec{B}$, which is the source term that generates motion of the fluid under study. Then, the equations of viscous flow and the Lorentz force are coupled to describe the flow dynamics of an electrically conducting fluid subjected to electromagnetic interaction. In the third section, the equations that govern the low Reynolds number flows of electrically conducting fluids are introduced in non–dimensional form. Moreover, the low magnetic–Reynolds number approximation ($R_m \ll 1$) is satisfied because the conductivity of most electrolytes is very weak compared to that of liquid metals, making all induced effects owing to the motion of the electrolyte under the applied magnetic negligible.

2.1 Equations of viscous flow

When the volume of a fluid remains unchanged, the fluid is said to be incompressible, and thus its density can be considered constant. The electrolyte used in this work is assumed to be of constant density, and therefore, the equation of continuity is simply

$$\nabla \cdot \vec{u} = 0, \tag{2.1}$$

where $\vec{u}$ is the velocity field vector, which is in general a spatiotemporal dependent vector.

For a Newtonian fluid, like most electrolytes and liquid metals are, the fluid is governed by the Navier–Stokes equation, that is,

$$\frac{\partial \vec{u}}{\partial t} + (\vec{u} \cdot \nabla)\vec{u} = -\frac{1}{\rho}\nabla P + \nu \nabla^2 \vec{u} + \frac{1}{\rho}\vec{f}, \tag{2.2}$$

where ρ is the density of the fluid, P is the pressure field, ν is the kinematic viscosity of the fluid, and $\vec{f}$ is a vector representing any body force that acts upon the fluid.

The motion of the fluid considered in this work is produced by electromagnetic stirring, that is, due to a force created by the interaction of an applied electric current and an imposed magnetic field, which we call the Lorentz force.

2.2 Ohm's law and the Lorentz force in a continuous medium

The field of electrodynamics has an extensive theory and numerous applications, particularly those related with the interaction of electrically conducting fluids and electromagnetic fields. In this section, we summarize the physical laws that lead to the derivation of the Lorentz force in a continuous conducting medium.

A charged particle q moving with velocity $\vec{u}$ inside a magnetic field $\vec{B}$, will be, in general, subject to three electromagnetic forces $\vec{f} = q(\vec{E}_s + \vec{E}_i + \vec{u} \times \vec{B})$. The first term $q\vec{E}_s$, is the electrostatic force that arises from the mutual repulsion or attraction of electric charges. In the second term, $q\vec{E}_i$ is the force experienced by the charged particle in the presence of a time varying magnetic field, where $\vec{E}_i$ is the induced electric field due to the changing magnetic field. The third term $q(\vec{u} \times \vec{B})$ is the magnetic force, which arises from the movement of the charged particle inside a magnetic field $\vec{B}$. For convenience, the total electric field shall be defined as $\vec{E} = \vec{E}_s + \vec{E}_i$, and $\vec{f}$ can be rewritten as

$$\vec{f} = q(\vec{E} + \vec{u} \times \vec{B}), \tag{2.3}$$

which is conventionally referred to as the Lorentz force that acts on a charged particle moving through a magnetic field (Davidson 2017).

In the case of a stationary electrical conductor, the current density $\vec{J}$ will be proportional to the force experienced by the free charges, and this can be expressed through Ohm's law as

$$\vec{J} = \sigma\vec{E}, \tag{2.4}$$

where σ is the electrical conductivity of the material and $\vec{E}$ is the electric field in a fixed frame of reference, that is, a frame in which the charges are instantaneously at rest. For the case of a fluid moving with velocity $\vec{u}$ with respect to the laboratory frame, Ohm's law takes the form

$$\vec{J} = \sigma(\vec{E} + \vec{u} \times \vec{B}), \tag{2.5}$$

where the fields in the fixed and laboratory frames are related by

$$\vec{E}^* = \vec{E} + \vec{u} \times \vec{B}. \tag{2.6}$$

Magnetohydrodynamics is primarily concerned with the bulk force acting on the continuous medium, rather than the forces affecting individual charges. Taking the sum over a unit volume of the conductor from equation (2.3), $\sum q$ becomes the charge density ρ_e, $\sum q\vec{u}$ becomes the current density $\vec{J}$, and equation (2.3) now becomes the volumetric Lorentz force

$$\vec{F} = \rho_e\vec{E} + \vec{J} \times \vec{B}, \tag{2.7}$$

where $\vec{F}$ is the electromagnetic force per unit volume acting on the conductor. However, when working with fluids such as electrolytes driven by the interaction of electric currents and applied magnetic fields, the first term of equation (2.7) is negligible (Figueroa $et\ al.$ 2009), hence the force takes the simplified form

$$\vec{F} = \vec{J} \times \vec{B}, \tag{2.8}$$

which is generally known as the Lorentz force.

2.3 Equations of magnetohydrodynamics

The motion of liquid metals and other working fluids of high electrical conductivity under the interaction of strong magnetic fields will give rise to induced electrical currents that in turn modify the applied magnetic field. Then, the total current density, $\vec{J}$, and the total magnetic field, $\vec{B}$, will be the sum of the applied plus the induced contributions, that is, $\vec{J} = \vec{j}^0 + \vec{j}^i$, and $\vec{B} = \vec{B}^0 + \vec{b}$ respectively, where $\vec{j}^0$ and $\vec{B}^0$ are the applied current density and magnetic field, while $\vec{j}^i$ and $\vec{b}$ are the induced contributions. However, when working with electrolytes whose electrical conductivity is very small compared to that of liquid metals, all induced effects related to the motion of the conducting fluid under an applied magnetic field are negligible (Figueroa $et\ al.$ 2009). There are two important dimensionless parameters that play an important role in MHD, the Hartmann number and the magnetic Reynolds

number. The Hartman number, defined as $Ha = dB_0\sqrt{\sigma/\rho\nu}$, estimates the ratio of the magnetic forces and the viscous forces, while the magnetic Reynolds number, $R_m = \mu_0\sigma U_0 d$, estimates the ratio of the magnetic field induced by the electric currents and the applied magnetic field, where d is a characteristic length of the flow. In our experimental problem, due to the small scale and the low electrical conductivity of the electrolyte, both parameters are much less than unity. It can be shown (Figueroa *et al.* 2009) that under these conditions all induced effects can be neglected, therefore, it is not necessary to consider the whole set of electromagnetic equations coupled with the fluid dynamic equations.

In problems where electrolytes are driven by Lorentz forces created by the interaction of injected electric currents and applied magnetic fields, as it is the case in the present study, it is sufficient to include this force in the equations of motion to consider the full electromagnetic interaction. In fact, this force is completely known since both the injected electric current and the applied magnetic field are given from the beginning.

In order to describe the flow of an electrolyte, the last right hand term of equation (2.2) must be substituted with the Lorentz force in the form of equation (2.8) to take into account the effects of the applied body force. As follows, the Navier–Stokes equation becomes

$$\frac{\partial \vec{u}}{\partial t} + (\vec{u} \cdot \nabla)\vec{u} = -\frac{1}{\rho}\nabla P + \nu\nabla^2\vec{u} + \frac{1}{\rho}(\vec{J} \times \vec{B}), \tag{2.9}$$

which must be complemented by the continuity equation (2.1).

2.3.1 Non–dimensionalization

We now proceed to express in dimensionless terms the governing equations of motion, assuming that the properties of the electrolyte such as the density, viscosity and electrical conductivity are constant and known for the working fluid. In addition, the injected current density $\vec{j^0}$ and the applied magnetic field, $\vec{B^0}$, are parameters controlled externally that modify the outcome of the experiment. With this premise, a dimensional analysis using the following variables was performed, where subscript $()_0$ in the variables represents a characteristic value and superscript $()^*$ denotes a dimensionless variable:

$$\vec{u^*} = \frac{\vec{u}}{u_0}, \quad P^* = \frac{P}{\rho u_0^2}, \quad \vec{x^*} = \frac{\vec{x}}{d}, \quad t^* = \frac{t}{d^2/\nu}, \quad u_0 = \frac{\nu}{d}, \quad \nabla^* = \nabla d, \quad \vec{J^*} = \frac{\vec{J}}{J_0}, \quad \vec{B^0} = \frac{\vec{B}}{B_0}.$$

The characteristic magnetic field B_0 is generally depicted as B_m which represents the maximum magnetic field intensity offered by the permanent magnet used. The characteristic length of the system is d, which in our case is the size of the magnet and $u_0 = \nu/d$ is a viscous velocity.

By substituting the non–dimensional variables in equations (2.1) and (2.9), and dropping the asterisk notation $()^*$ for simplicity, the following system of non–dimensional equations is obtained:

$$\nabla \cdot \vec{u} = 0, \tag{2.10}$$

$$\frac{\partial \vec{u}}{\partial t} + (\vec{u} \cdot \nabla)\vec{u} = -\nabla P + \nabla^2\vec{u} + Re(\vec{J^0} \times \vec{B^0}), \tag{2.11}$$

$$\nabla \cdot \vec{B^0} = 0, \tag{2.12}$$

$$\nabla \times \vec{B^0} = 0. \tag{2.13}$$

Equation (2.10) expresses the conservation of mass; equation (2.11) describes the balance of momentum with the Lorentz force as the main body force; equation (2.12) expresses the solenoidal nature of the applied magnetic field; and equation (2.13) depicts the irrotational character of the applied magnetic field.

The Reynolds number, $Re = U_0 d/\nu$, in equation (2.11) estimates the ratio of convective forces to viscous forces. It is important to recall that in equation (2.9), the balance of viscous and electromagnetic forces results in $|\nu \nabla^2 \vec{u}| \sim |(\vec{J} \times \vec{B})/\rho|$. From this balance, the order of magnitude relation $\nu U_0/d^2 \sim J_0 B_0/\rho$ is obtained, which results in $U_0 = J_0 B_0 d^2/\rho \nu$, where U_0 is the characteristic velocity that results from the balance of viscous and Lorentz forces.

2.3.2 Two–dimensional (2D) approximation

There are a number of reasons as to why a fluid dynamics experiment can be studied using a 2D approach in a 3D world. For a homogeneous fluid under angular rotation, motions parallel to the axis of rotation (out–of–plane) are suppressed by the constraint of the rotating motion. When the fluid is stratified under a gravitational field, fluid motions will be inhibited due to the work that must be done to overcome the force of gravity (Veronis 1970). Additionally, in liquid metal flows, imposed magnetic fields tend to destroy gradients of velocity $\vec{u}$ parallel to $\vec{B}$. This happens when fluid motion across magnetic field lines induces a current, leading to a rise in thermal energy owing to Joule dissipation, which in turn causes the extinction of mechanical energy (Davidson 2017). In the case of the experiments in the present work, the aspect ratio of the horizontal extent to the vertical depth is large, which makes two–dimensionality a reasonable approach.

Taking these considerations into account, a 2D model was chosen which ignores any dependence on the vertical z coordinate, so the velocity field is now $\vec{u} = [u(x, y, t), v(x, y, t), 0]$. The applied magnetic field is also assumed to be independent of the z coordinate, making $\vec{B} = [0, 0, B_z^0(x, y)]$. The applied current that flows across the x coordinate is uniform, which in dimensionless terms is taken as $j_x^0 = 1$. Therefore, under this approximation, the system of equations that governs the motion of the electrolyte acted by the applied Lorentz force is the following:

$$\frac{\partial u}{\partial x} + \frac{\partial v}{\partial y} = 0, \tag{2.14}$$

$$\frac{\partial u}{\partial t} + u\frac{\partial u}{\partial x} + v\frac{\partial u}{\partial y} = -\frac{\partial P}{\partial x} + \frac{\partial^2 u}{\partial x^2} + \frac{\partial^2 u}{\partial y^2}, \tag{2.15}$$

$$\frac{\partial v}{\partial t} + u\frac{\partial v}{\partial x} + v\frac{\partial v}{\partial y} = -\frac{\partial P}{\partial x} + \frac{\partial^2 v}{\partial x^2} + \frac{\partial^2 v}{\partial y^2} - Re B_z^0. \tag{2.16}$$

This system of equations will be used in Chapter 4 to obtain approximate analytical and numerical solutions of the electromagnetically driven flow of interest.

Chapter 3

Experimental methodology

In this chapter, the characteristics of the experimental setup and methodology are described. The experiment was designed to stir an electrolyte at a millimetric scale using the Lorentz force, which was generated by the interaction of an electric current and the magnetic field created by one or more permanent magnets. The first section offers a general introduction of the experimental stage. The second section describes the characteristics of the experimental cell and the essential components involved in the experiments, such as the magnets and the composition of the electrolyte. Finally, the last sections describe the particle image velocimetry procedure, which is used to obtain velocity fields by tracking particle tracers in the flow, and the long exposure photography procedure, which is used to capture the streamlines traced by the particle tracers.

3.1   Introduction

Both theoretical and laboratory groundwork regarding electromagnetically driven vortices of electrolyte in shallow layers were initially performed twenty years ago by Salas *et al.* (2001) in the fluid mechanics group at the *Centro de Investigación en Energía* (CIE) [IER in the present time]. In their experiment, black and white photographs (see figure 3.1(a)) were captured of the flow pattern developed after applying a steady electrical current inside a 40 cm × 20 cm × 2 cm plexiglass box. Further experiments and numerical simulations for similar configurations were carried out by Figueroa *et al.* (2009) (see figure 3.1(b)), where a 28 cm × 36 cm × 1.6 cm plexiglass and glass box was built in order to analyze depth-dependent velocity profiles using particle image velocimetry. Both configurations involved a permanent magnet of about 2.5 cm of diameter under the bottom wall.

In order to compare the theoretical and experimental results, several parameters are needed, mainly a characteristic length d (typically the diameter of the magnet), the depth of the electrolyte layer h, the applied electric current in mA, the Re number and the volume of fluid in cm^3. In the present study, the size of experimental setup was lowered in an order of magnitude with respect to previous experimental analyses. A magnet of 1.5 mm in diameter was used, and the domain of the flow under observation was drastically reduced to a millimetric scale in order to visualize flow patterns inside a 10 mm × 10 mm region. This information is summarized in table 3.1.
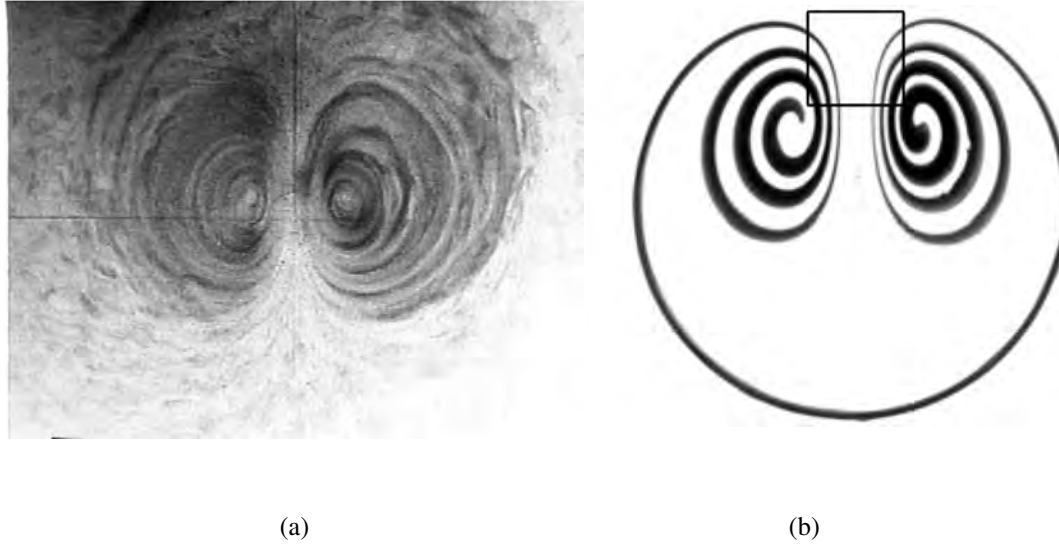
(a)   (b)

FIGURE 3.1: **(a)** Dipolar flow pattern obtained by Salas *et al.* (2001) using DC current. **(b)** Experimental dye visualization of a steady dipolar vortical structure generated with DC current by Figueroa *et al.* (2009).

TABLE 3.1: Experimental parameters[†] from previous works.

	d [cm]	h [cm]	domain size [cm]	mA	*Re*	cm³
Salas *et al.* (2001)	2	0.6	40×20×2	40 to 150	10	480
Figueroa *et al.* (2009)	1.9	0.4	28×36×1.6	10 to 100	100*	400
This work	0.15	0.1	5.4×1.9×0.1	1 to 10	4	1

All experiments were performed using an electrolytic solution of water and sodium bicarbonate. [†]Units correspond to those reported in the papers. *Approximate value.

The reduction of the domain introduces important effects on the overall experimental conditions, particularly on the Reynolds number *Re*, the main parameter which controls the global flow. In fact, note that the last right hand term of equation (2.11) is proportional to $Re = U_0 d / \nu$. Macroscopic experiments in the laboratory will typically result in values of $Re \sim 10^3$, whereas industrial scale experiments and natural phenomena will result in values of $Re \sim 10^6$, or even higher for geophysical and astrophysical events. For these reasons, the value of *Re* deserves special attention when performing numerical simulations, because very high values will lead to instabilities or even turbulence. On the other hand, in our normalization the condition $Re = 0$ corresponds to the absence of the Lorentz force in equation (2.11) and, therefore, to the absence of motion.

Additional considerations can arise when the domain of the experiment is altered. When working with shallow layers of electrolyte in a laboratory, the condition of a horizontal extent that largely exceeds the vertical extent must be satisfied so that a two dimensional approximation can be safely assumed. When the layer is too thick, three dimensional (3D) effects become relevant and different approaches are needed to describe the dynamics of the flow. When the layer is shallow, viscous effects from the bottom wall are significant, and these effects will become

more important as the thickness of the layer decreases.

In spite of this, due to physical conditions, a two dimensional approach will always be exclusively theoretical as 3D effects are intrinsic to real flow structures (Akkermans *et al.* 2008; Martell *et al.* 2019). In the present study, an electrolyte composed of water and NaHCO$_3$ is used as the working fluid. This solution is characterized by having low electrical conductivity compared to that of liquid metals and common copper conductors. Therefore, when applying an electric current, care must be taken to avoid overloading the electrolyte, because one or more of the following issues may occur: a) direct current flowing across copper electrodes will create an oxidation byproduct which will detach from the cathode into the electrolyte, turning it into a light green–blue color. In large cells this will not be an immediate problem, but small cells will quickly saturate with the byproduct, complicating the visualization and compromising the performance of the experiment. This phenomenon can be lessened using chromed electrodes (Salas *et al.* 2001), or by reducing the intensity of the current; b) Joule heating, the phenomenon through which thermal energy is produced as a result of current flow, will occur (on a much smaller scale) in the electrolyte; resulting in an electrical conductivity decrease proportional to the Ohmic losses. This phenomenon may also affect the hardware, for example, steady current sources fix their output by increasing or decreasing the voltage according to the resistance, as stated by Ohm's law. In the electrolyte, resistance build–up is expected as the experiment is in progress, so if the source is unable to sustain the desired output due to insufficient voltage, then a source with higher capacity will be required, and these are very expensive; c) Working with shallow layers is commonly associated with laminar flow, and very high currents can lead to destabilization of the flow, making the flows time–dependent, which can lead to chaos, thereby making experiments non–reproducible, as well as no longer valid on a purely two–dimensional approach due to the appearance of 3D effects (Kelley & Ouellette 2011).

On the other hand, on a shallow layer, even in the smallest cell, if the input current is too low, the Lorentz force will be very weak and unable to overcome viscous friction, in turn forcing effects or any flow patterns will be imperceptible.

3.2   Cell characteristics

A small cell was designed and built in order to visualize flow patterns confined to a region of millimetric dimensions. The cell was an ensemble of magnets, glass, plexiglass and copper (see figure 3.2(a)). The main components of the cell and a representation of the flow visualization region are shown in figure 3.2(b). The magnets are HKCM$^{®}$ grade N48 permanent dipolar magnets, made of a neodymium–iron–boron (NdFeB) alloy with a nickel coating that makes them resistant to humidity. The magnets have a cylindrical shape and are axially polarized, with 1.5 mm diameter and 0.5 mm height. As all magnetic dipoles, the magnets produce a field which decays across the axial distance from the geometrical center of the magnet to its border circumference.

The glass component is a standard 75 mm × 25 mm × 1 mm microscope glass slide. The brown colored components are electrodes, 60 mm × 5 mm length and width, and approximately 0.3 mm in height, with 20 mm in exceeding length on one of the sides to allow the connection between a DC voltage source and the experimental cell. The top component is a rectangular plexiglass enclosing designed to confine the electrolyte in a pool–like configuration with a maximum vertical depth of 1 mm, making this the height of the electrolyte layer (see figure 3.2(c)). The dimensions of the pool are then 54 mm × 19 mm × 1 mm.

The electrodes were glued directly on top of the glass slide using Resistol$^{®}$ 911 Flex Gel[1] and the plexiglass confinement sat on top of the electrodes. The electrodes are originally 5 mm wide but only 2 mm came in direct contact with the electrolyte. This specification originated from the effect of electrolysis: a larger contact area allowed for more copper oxide production, whereas a smaller contact area helped to reduce this effect. This, however, did not compromise the experiment due to the low input current.

---

[1]After intensive experimentation with many products such as modeling clay, hot glue, UHU$^{®}$, and Kola Loka$^{®}$ both in its solid and liquid forms; Resistol$^{®}$ 911 Flex Gel presented impermeability, great resistance to electrochemical wear, and exceptional tolerance to constant shearing stress induced by wiping and sanding.
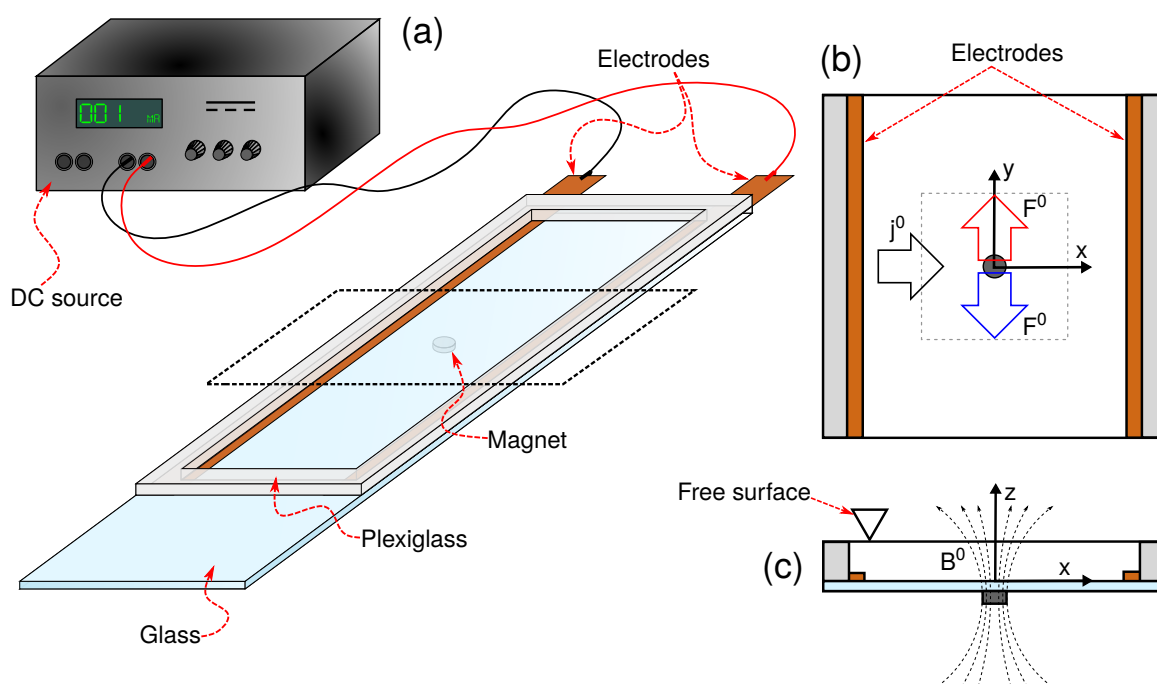
FIGURE 3.2: Experimental set up[†]. **(a)** perspective view of the experimental cell connected to the DC source (not drawn to scale). The black dashed lines correspond to **(b)** a representation of the visualization area where the gray dashed lines indicate an approximate region where the main flow occurs. **(c)** front view indicating the free surface of the electrolyte layer. The applied electrical current and magnetic field are denoted by j^0 and B^0, respectively. The Lorentz force is denoted by F^0, where the blue and red arrows indicate positive and negative polarization of the magnet, respectively. [†]Refer to appendix A for an annotated illustration of the experimental cell.

The electrolyte is a solution of water and sodium bicarbonate ($NaHCO_3$) at 8.6% in weight. The components were placed on a 200 ml beaker and permanently agitated on an electromagnetic stirrer at low speed to prevent crystallization.

Geometrical magnet arrangements have been previously studied for alternating current on larger cells and with the objective of visualizing time dependent flows (Figueroa *et al.* 2011; Figueroa *et al.* 2014). The present experiment focused on visualizing the steady state flow. A velocity field for each geometrical arrangement was obtained by averaging multiple frames per second of footage, and the path of the tracers was captured using long exposure photography. Experimental results were ultimately compared with analytical and numerical solutions. The different magnet arrangements are shown in figure 3.3.

FIGURE 3.3: Geometrical shapes used to arrange the magnets. **(a)** center, **(b)** square, **(c)** hexagon, and **(d)** checkerboard–magnet arrangement. Blue and red represent north and south poles of the magnet, respectively.

3.3 Particle image velocimetry

Experimental observations using particle image velocimetry, commonly referred to as PIV, can be performed in multiple ways according to the purpose of the study; in this case we observe the cell only from above in a planar configuration. Laser light sheets are frequently used to illuminate the desired plane of view. However, given the experimental characteristics of the small cell in the present study, topside illumination using LED lamps was adequate.

The LED lamps were supported by laboratory stands, placed along an imaginary axis perpendicular to the lens with the diameter of the lens acting as the distance separating each lamp. The lamps were placed adjacent to the filter thread, across from each other at a 45° and 135° inclination angle with respect to the imaginary axis, so that the light beams intersected at a 90° angle directly below the lens (see figure 3.4). Luminous intensity and light scattering due to the proximity of the lamps with the lens were addressed pragmatically by dimming the lamps with with white paper sheets. To enhance the contrast of the particles, the bottom of the glass slide was coated in a uniform layer of mate black paint and the footage was recorded in an otherwise dark space in order to avoid dispersed light and reflections from the ceiling lamps. Topside illumination is adequate in our experimental setup since the area of interest is solely on the free surface.
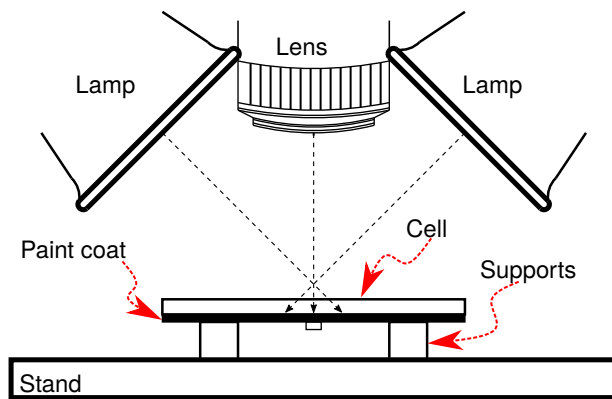

FIGURE 3.4: Lighting setup. The paint coat was overly depicted to highlight its place in the experimental setup; its thickness was not determined but was still much thinner than the height of the magnet (0.5 mm). Given that the glass slide is completely flat and magnets are glued to the bottom, supports were placed to guarantee horizontal evenness of the shallow layer.

The flow footage was captured with an HDSLR type Nikon® D7100 camera which was mounted on a tripod 12 cm above the fluid layer. Due to the slow velocity of the flows under study there was no need for excessive temporal detail, therefore the camera was adjusted to film at a progressive frame rate of 30 fps with a resolution of (1920×1080) pixels (px). An AF-S VR Micro-Nikkor 105mm f/2.8G IF-ED lens was used, where the long focal length was helpful in obtaining a naturally narrow field of view of the 10 mm $\times$ 10 mm region. The aperture of the lens was fixed at f/5.6 to dim incoming light from the lamps and to enhance the contrast of the reflected light from the particles. The depth of field was not determined since the specific objective of the experiment was placed on capturing the flow dynamics exclusively at the surface of the cell, however it is expected to be very shallow, around an estimated 0.5 mm to 1 mm.

The electrolyte layer was seeded with Dantec Dynamics® HGS–10 particles, which are hollow borosilicate glass spheres with a mean particle diameter of 10 μm. The ratio of particles to the volume of fluid (1 cm^3) could not be quantified, therefore, the particles were manually added to the fluid trying to be as consistent as possible in all the experiments.

Dry particles were seeded to the electrolyte and the tip of a syringe was used to agitate the particles. Then, the fluid was left still to let it reach a state of rest which happened in about 10 seconds due the high viscous coupling from the bottom. The relaxation period was also used to let denser particles sediment, which lasted a minute or more, in an effort to remove them and avoid visual interferences when filming. This strategy also consisted in suctioning the sedimented particles from the glass floor using the syringe; but the micrometric size of the particles made it very difficult and the millimetric thickness of the layer immediately decreased while pulling on the plunger. The sedimentation step of this strategy was ultimately eliminated and instead, the camera was focused exclusively on the particles at the free surface. At this point, it was noticed that in the short relaxation time of 10 seconds, particles were forming clusters, and the density of the clusters increased with time. This effect also intensified as

the electric current was driven through the fluid (see §5.6). It can be hypothesized that particle clusterings were being caused by surface–tension–driven interactions (Vella & Mahadevan 2005). Although surface tension affects flow motion at any extent, its effects can be more meaningful at small scales.

For the velocimetry procedure, videos of up to one or more minutes of continuous forcing were recorded and the camera was controlled electronically through tethered shooting software[2]. The footage was analyzed on the computer and 10 seconds were selected for the velocimetry analysis. The first seconds of the transitory phase to steady flow in the videos were discarded. The time after the 10 seconds intervals were also eliminated from the analysis because electrochemical effects began to take over the flow and no more movement could be appreciated (see §5.6).

For each magnet arrangement, 300 image pairs were extracted and were processed with the PIVLab[3] toolbox from MATLAB®. Four passes were used on all image pairs to ensure maximum precision. The interrogation areas (IA) were selected in function of the particle density making sure that the recommended 5 to 20 particles were inside the IAs at all times. Due to the augmented size of the particles, we were able to safely use a fourth pass without introducing high noise levels and erroneous correlations. The slow flow also played an important role in harvesting high resolution results given the slow spatiotemporal deformation of the grid used in the velocimetry analysis. High Reynolds number flows and turbulent flows tend to yield plenty of spurious vectors, also known as outliers, that have to be dealt with using additional tools such as smoothing or manual removal. In our case, a very low yield of outliers was addressed through an outlier detection test based on Westerweel and Scarano (2005) that is readily implemented in the PIVLab toolbox.

The regions of interest (ROI) were selected accordingly with the magnetic distribution under study. Regions where flow patterns were distinguishable were selected as ROI to speed up computation time, and most importantly, because flow velocities tend to zero outwards from the center of the magnet and drop to zero at the plexiglass borders satisfying the no–slip condition. For all image pairs analyzed and in accordance with experimental parameters, the calibration values were the same characteristic length $d = 1.5$ mm, as well as the time step $\Delta t = 33$ ms, being this the elapsed time in between frames.

3.4 Long exposure photography

There are three widely known experimental approaches to visualize a flow patterns: streaklines, pathlines, and streamlines. A streakline is a line that joins particles which pass through a particular point in the fluid; this is commonly realized by continuously injecting a fluid tracer on a fixed point of the domain. The fluid tracer can be an organic colorant like food dye, or other substances that are non–intrusive to the flow. A pathline is the locus of points that a particle outlines as it moves with the flow. One way to visualize pathlines is by seeding particle tracers to the fluid and following them as they drift with the flow. A streamline is a curve tangential to instantaneous velocity vectors in the flow, thus its concept is fundamentally mathematical in nature (Kline 1969). However, streamlines can be observed by following particles of a seeded fluid as they wander with the flow, where the streamlines will be the curves traced by the particles during a specific time interval.

For steady flows, all three flow lines are equivalent since the velocity field does not change with time, hence the results will be identical. In the case of a time dependent flow, all the three flow lines will differ as a result of a constantly changing velocity field. However, for such case, streamlines can be obtained by capturing particles along short time intervals and recovering their trajectories over multiple exposures. On the other hand, the pathlines can be obtained through the same procedure but with longer exposure times. This can be cumbersome for turbulent flows, therefore different approaches should be taken.

---

[2]The software is *digiCamControl*, a free, open–source application that runs on Windows and works for taking pictures and recording video. Refer to http://digicamcontrol.com/ for more information.

[3]Refer to Thielicke (2014), Thielicke and J. Stamhuis (2019), and Thielicke and Stamhuis (2014) for information on the toolbox and the download link.

Another frequented method for the case of steady flows is the injection of hydrogen bubbles resulting from electrolysis of a very thin wire placed inside the fluid. This method is effective because bubbles are very small, therefore, intrusive effects can be safely neglected. When using particle tracers, like in the present work, care should be taken to avoid inertial movement of the particles relative to the flow by using particles small enough so that these can be transported accurately by the carrier flow.

For our experiments, the cell depicted in figure 3.2 with the lighting setup depicted in figure 3.4 was used, with the slight modification that the lens was placed 4 cm above the cell. The same hollow glass spherical particles were used on a slightly lower proportion.

The same digital camera was used with an AF-S Micro-Nikkor 60mm ƒ/2.8G ED lens, where the short focal length allowed to capture a larger field of view of the flow region, which remained under 1.5 cm^2. The lens aperture was fixed at ƒ/10.0 to minimize light reflections as much as possible, and the sensitivity of the image sensor to light was set at the recommended ISO 100 to achieve a finer grain in the results. The exposure times were selected at 8 and 10 seconds, and the photographs had a resolution of 6000 px × 4000 px. Ultimately, all the photographs were digitally edited to eliminate unintended noise and to enhance contrast and definition.

Chapter 4

Theoretical model

In the first section of this chapter, a mathematical model is developed to solve equation (2.11) using a 2D approach. The equations are linearized with an asymptotic expansion on the *Re* number, which is known as the perturbations method, and then, Green's function method is used to obtain a solution to the equations. It can be shown that second and higher order terms in the asymptotic expansion can be neglected due to their very small contribution (Figueroa 2006), therefore, the solutions presented here are truncated to a first order approximation. The second section addresses the finite difference method which was used for the numerical simulation.

4.1 Analytical solutions for the low Reynolds number approximation

We start by presenting a first approach to the determination of the flow field in a thin layer of electrolyte produced by the Lorentz force created by the interaction of a uniform constant electric current and a dipolar magnetic field. With the aim of getting an analytical solution, we assume that the flow is purely two–dimensional, so that the interaction with the bottom confining wall and the top free surface is neglected. Under the conditions, the equations governing the flow are precisely the ones presented at the end of Chapter 2. Refer to figure 4.1 for an illustration of the theoretical model which helps to set up the analytical solution.

By taking the curl of the Navier–Stokes equations (2.15) and (2.16), the vorticity transport equation is obtained, namely,

$$\frac{\partial \omega}{\partial t} + u \frac{\partial \omega_z}{\partial x} + v \frac{\partial \omega_z}{\partial y} = \frac{\partial^2 \omega_z}{\partial x^2} + \frac{\partial^2 \omega_z}{\partial y^2} - Re \frac{\partial B_z^0}{\partial x}, \tag{4.1}$$

where $\omega_z = \frac{\partial v}{\partial x} - \frac{\partial u}{\partial y}$ is the only vorticity component. Equation (4.1) can be rewritten in a compact form using vector notation

$$\frac{\partial \omega_z}{\partial t} + (\vec{u} \cdot \nabla)\omega_z = \nabla^2 \omega_z - Re \frac{\partial B_z^0}{\partial x}. \tag{4.2}$$

In equation (4.2), the first term in the left–hand side represents the temporal dependence of vorticity. The second term expresses vorticity advection by the flow, while the first term on the right–hand side expresses the viscous diffusion of vorticity. In turn, the second term of the right–hand side represents the action of external forces, which in this case corresponds to the electromagnetic source (curl of the Lorentz force) that produces vorticity in the flow.

For the sake of simplicity, we assume that the applied magnetic field is given by a magnetic point dipole for which an analytical expression exists. The analytical expression for the magnetic field is taken from Good and Nelson (1971), and since the modeling is tailored for a 2D approach, only the component along the normal
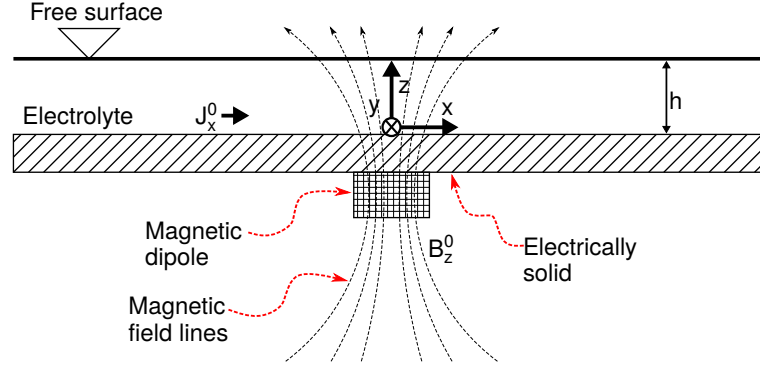
FIGURE 4.1: Theoretical model. The applied electric current and magnetic field are denoted by J_x^0 and B_z^0, respectively.

z–coordinate is taken. This results in a magnetic dipole whose magnetic moment $\mathbf{m} = m\hat{k}$ points normal to the xy plane, and whose normal component in dimensional terms is expressed as

$$B_z^0(x, y) = \frac{\mu_0}{2\pi} \frac{m}{x^2 + y^2} + \mu_0 m \delta(x)\delta(y). \tag{4.3}$$

The first term on the right hand side of equation (4.3) estimates the magnetic field everywhere outside of the origin $(x^2 + y^2 \neq 0)$, while the second term accounts for the singularity of the field and is represented by the Dirac delta function, which estimates the value of the magnetic field at all places where the function is valued at zero. To non–dimensionalize the expression for the magnetic field, B_z^0 can be normalized with $B_m = \mu_0 m / L^2$, where the characteristic length L can be chosen as $L = \sqrt{\mu_0 m}$ so that the normalization constant $\mu_0 m / L^2$ takes a value of 1 (Cuevas *et al.* 2006a). The dimensionless expression for the magnetic field is then

$$B_z^0(x, y) = \frac{1}{2\pi} \frac{1}{x^2 + y^2} + \delta(x)\delta(y). \tag{4.4}$$

It is worthwhile noting that the full 3D expression of the magnetic field satisfies magnetostatic equations (2.12) and (2.13), and since equation (4.4) losses its irrotational nature, the magnetostatic equations will not be completely satisfied. However, the expression provides a proper description of the magnetic field given that the contributions of the field are very small along x and y. For magnets that are distributed outside the origin, the following expression can be used

$$B_z^0(x, y) = \frac{1}{2\pi} \frac{1}{(x - x_0)^2 + (y - y_0)^2} + \delta(x - x_0)\delta(y - y_0), \tag{4.5}$$

where (x_0, y_0) are the coordinates of the position of the magnet.

4.1.1 Boundary conditions and initial conditions

The solution assumes that the fluid is at rest as initial condition. Owing to the small magnet size and the large extent of the electrolyte layer, the boundary conditions for the single magnet and the magnet superposition have been selected as if it were the case of an infinite domain and have been chosen as follows. At the origin of the magnet, the velocity field and the pressure field must take a finite value. The magnetic field decays outwards from the origin of the magnetic field, therefore at a distance far enough from the magnet, the Lorentz force term will decrease proportionally, resulting in a very small (negligible) contribution. For the case of magnet superposition, the conditions state that the velocity in the neighborhood of the magnets must take a finite value. On the other hand, at a distance R far enough from the center of the magnets, the velocity can be assumed to be zero, where the distance from the center of the magnets to a given point in space is calculated as $r = \sqrt{x^2 + y^2}$.

<div align="center">

Single magnet   Magnet superposition

</div>

$$\left.\begin{array}{l} u \to \text{finite} \\ v \to \text{finite} \\ P \to \text{finite} \end{array}\right\} x, y \to 0, \qquad\qquad \left.\begin{array}{l} u \to \text{finite} \\ v \to \text{finite} \\ P \to \text{finite} \end{array}\right\} r \to 0,$$

$$\left.\begin{array}{l} u \to 0 \\ v \to 0 \\ P \to \text{const.} \end{array}\right\} x, y \to \pm\infty, \qquad\qquad \left.\begin{array}{l} u \to 0 \\ v \to 0 \\ P \to \text{const.} \end{array}\right\} r \to R,$$

$$\left.\begin{array}{l} u = v = 0 \\ P \to \text{const.} \end{array}\right\} t = 0. \qquad (4.6) \qquad\qquad \left.\begin{array}{l} u = v = 0 \\ P \to \text{const.} \end{array}\right\} t = 0. \qquad (4.7)$$

4.1.2 Solution by perturbations method

Taking into account the main assumption of the Reynolds number being very small, a perturbations method has been used searching for a solution as a power series expanded on the small parameter Re, where the superscript in the variables indicates the order of approximation,

$$\omega_z = \omega_z^{(0)} + Re\,\omega_z^{(1)} + Re^2\omega_z^{(2)} + \mathcal{O}(Re^3),$$
$$u = u^{(0)} + Re\,u^{(1)} + Re^2 u^{(2)} + \mathcal{O}(Re^3),$$
$$v = v^{(0)} + Re\,v^{(1)} + Re^2 v^{(2)} + \mathcal{O}(Re^3). \qquad (4.8)$$

Zero[th]–order approximation

The vorticity equation approximated to zero[th]–order $\mathcal{O}(Re^0)$ reduces to

$$\frac{\partial \omega_z^{(0)}}{\partial t} + u^{(0)}\frac{\partial \omega_z^{(0)}}{\partial x} + v^{(0)}\frac{\partial \omega_z^{(0)}}{\partial y} = \frac{\partial^2 \omega_z^{(0)}}{\partial x^2} + \frac{\partial^2 \omega_z^{(0)}}{\partial y^2}, \qquad (4.9)$$

whose solution is

$$\omega_z^{(0)} = u^{(0)} = v^{(0)} = 0, \qquad (4.10)$$

due to the absence of a source term generating motion in the fluid.

First–order approximation

To a first order approximation, the vorticity equation satisfies

$$\frac{\partial \omega_z^{(1)}}{\partial t} = \frac{\partial^2 \omega_z^{(1)}}{\partial x^2} + \frac{\partial^2 \omega_z^{(1)}}{\partial y^2} - \frac{\partial B_z^0}{\partial x}, \qquad (4.11)$$

where equation (4.11) takes the form of a diffusion equation with an external source, which comes from the Lorentz force term. The Green's function method (Hahn & Özişik 2012) was used to solve equation (4.11) on an infinite domain $-\infty < x < \infty$, $-\infty < y < \infty$ for all $t > 0$, along with the initial condition $\omega_z^{(1)} = 0$ for $t = 0$. It turns that the Dirac delta term in equation (4.4) is the only term whose contribution to the solution is greater than zero. Finally, the first order time–dependent solution is

$$\omega_z^{(1)} = -\frac{1}{2\pi}\frac{x}{x^2+y^2}e^{-\left(\frac{x^2+y^2}{4t}\right)}. \qquad (4.12)$$

The steady state solution can be obtained by evaluating equation (4.12) in the limit when $t \to 0$, which results in

$$\omega_z^{(1)} = -\frac{1}{2\pi} \frac{x}{x^2 + y^2}. \tag{4.13}$$

It can been seen from equations (4.12) and (4.13) that the solution will diverge at the origin, which is mainly due to the magnetic field expression which also diverges at the origin. Regardless of this, the results in Chapter 5 show that for both a single magnet and the superposition of magnets, the behavior of the results is qualitatively acceptable.

Once the vorticity is known, the stream function ψ is calculated by solving the equation

$$\nabla^2 \psi = -\omega_z, \tag{4.14}$$

where

$$u = \frac{\partial \psi}{\partial y}, \quad \text{and} \quad v = -\frac{\partial \psi}{\partial x}. \tag{4.15}$$

By considering a similar series expansion for the stream function

$$\psi = \psi^{(0)} + Re\psi^{(1)} + Re^2\psi^{(2)} + \mathcal{O}(Re^{(3)}), \tag{4.16}$$

at first order of approximation, the stream function satisfies the equation

$$\frac{\partial^2 \psi^{(1)}}{\partial x^2} + \frac{\partial^2 \psi^{(1)}}{\partial y^2} = -\omega_z^{(1)}. \tag{4.17}$$

The solution of equation (4.17) will be the sum of the homogeneous solution plus the particular solution, which can be solved by using polar coordinates assuming the solution is a product of functions: $\psi(r, \theta) = f(r) \cos(\theta)$. This makes equation (4.17) to take the form

$$\frac{1}{r} \frac{\partial}{\partial r} \left(r \frac{\partial \psi(r, \theta)}{\partial r} \right) + \frac{1}{r^2} \frac{\partial^2 \psi(r, \theta)}{\partial \theta} = -\frac{1}{2\pi} \frac{r \cos(\theta)}{r^2}, \tag{4.18}$$

and the final solution is found to be

$$\psi^{(1)}(r, \theta) = \frac{r \cos(\theta)}{8\pi}[1 - \log(r^2)] + \frac{C_1}{r} \cos(\theta) + C_2 r \cos(\theta), \tag{4.19}$$

$$\psi^{(1)}(x, y) = \frac{x}{8\pi}[1 - \log(x^2 + y^2)] + C_1 \frac{x}{x^2 + y^2} + C_2 x, \tag{4.20}$$

where equations (4.19) and (4.20) are the solutions in polar and Cartesian coordinates, respectively. The same solution is used for the case of a single magnet and for the superposition of magnets, however, each case will be solved individually in the sections below.

4.1.3 Flow generated by a single magnet

Boundary conditions for the single magnet case (equations (4.6)) require that constants of integration C_1 and C_2 in equation (4.20) to be zero, which results in

$$\psi^{(1)}(x, y) = \frac{x}{8\pi}[1 - \log(x^2 + y^2)]. \tag{4.21}$$

Using equation (4.15), the velocity components result in

$$u^{(1)} = -\frac{1}{4\pi} \frac{xy}{x^2 + y^2},$$

$$v^{(1)} = \frac{1}{8\pi} \left(\log(x^2 + y^2) + \frac{2x^2}{x^2 + y^2} - 1 \right). \tag{4.22}$$

4.1.4   Flow generated by the superposition of two or more magnets

Owing to the linearity of the problem under the low Reynolds number approximation, the solution for a single magnet can be superposed accordingly with the number of magnets desired; though, as will be shown, the interactions are not completely well replicated owing to the magnetic dipole expression. Still, the resultant velocity field is qualitatively acceptable and can be used as a first approximation.

Constants C_1 and C_2 in equation (4.20) are found by applying the boundary conditions from equations (4.7) to obtain

$$\psi^{(1)}(x, y) = \frac{x}{8\pi} \left[1 + \log\left(\frac{R^2}{x^2 + y^2} \right) - \frac{R^2}{x^2 + y^2} \right]. \tag{4.23}$$

Using equation (4.15), the velocity components result in

$$u^{(1)} = \frac{xy}{4\pi(x^2 + y^2)} \left[\frac{R^2}{(x^2 + y^2)} - 1 \right],$$

$$v^{(1)} = \frac{1}{8\pi} \left[\frac{2x^2}{x^2 + y^2} + \log\left(\frac{R^2}{(x^2 + y^2)} \right) - \frac{R^2(x^2 - y^2)}{(x^2 + y^2)^2} - 1 \right]. \tag{4.24}$$

The resulting superposition of magnets can be found analytically by specifying the coordinates of each magnet, for instance, in the case of a magnet located at (x_0, y_0), the velocity component $u^{(1)}$ takes the form

$$u^{(1)}(x, y) = \frac{(x - x_0)(y - y_0)}{4\pi((x - x_0)^2 + (y - y_0)^2)} \left[\frac{(x_0 + y_0)^2}{((x - x_0)^2 + (y - y_0)^2)} - 1 \right]. \tag{4.25}$$

As mentioned above, the superposition is expressed as

$$\psi^{(1)}(x, y) = \sum_{n}^{\infty} \psi^{(1)}(x_n, y_n), \tag{4.26}$$

where (x_n, y_n) represent the coordinates of the magnets.

4.2 Two dimensional numerical simulation

In the previous section, the analytical solutions pointed out to divergences originated from the singularities owing to the point dipole expression, which limits the capacity of the analytical solution to accurately replicate the experimental flow field. For such reason, a numerical solution is described in this section, which is performed by discretizing equation (2.11) using a finite differences method. This allows to take into account both the convective and diffusive terms. It is also designed to simulate a purely two–dimensional flow, thus ignoring the friction from the bottom wall. Some of the main advantages of the numerical solution are that it allows to analyze non–linear effects that appear at higher Reynolds numbers, as well as considering a realistic expression for the applied magnetic field.

4.2.1 Non–uniform applied magnetic field

The analytical solution is based on the assumption that the applied magnetic field is produced by an idealized magnetic point dipole. To improve this consideration, the numerical solution makes use of an analytical expression presented by McCaig (1977) to implement a non–uniform magnetic field of dipolar origin, where owing to the 2D approximation, only the normal–z component is considered. The analytical expression reproduces the field created by a magnetized rectangular plate uniformly polarized in the normal direction. The dimensions of the plate are $2a$ and $2b$ (taken as $a = b$ for practical purposes). Placing the coordinate system at the origin of the top surface of the magnet, the normal component of the magnetic field at a height z_0, created by a single magnetized plate is given by

$$B_z^0(x, y) = \xi B_m \left[\tan^{-1}\left(\frac{(x+a)(y+b)}{z_0\sqrt{(x+a)^2 + (y+b)^2 + z_0^2}} \right) \right.$$
$$+ \tan^{-1}\left(\frac{(x-a)(y-b)}{z_0\sqrt{(x-a)^2 + (y-b)^2 + z_0^2}} \right)$$
$$- \tan^{-1}\left(\frac{(x+a)(y-b)}{z_0\sqrt{(x+a)^2 + (y-b)^2 + z_0^2}} \right)$$
$$\left. - \tan^{-1}\left(\frac{(x-a)(y+b)}{z_0\sqrt{(x-a)^2 + (y+b)^2 + z_0^2}} \right) \right], \tag{4.27}$$

where ξ is a normalization parameter calculated from the maximum magnetic field intensity. Equation (4.27) approximates a symmetric distribution of the magnetic field whose maximum value is at the geometrical center of the plate. The intensity of the magnetic field decays outwards from the center of the plate.

For the numerical implementation, the magnetic field has been considered as the superposition of two parallel magnetized plates with opposing polarization separated by a distance ℓ. In this way, each plate represents the north and south poles of the permanent magnet (Figueroa *et al.* 2009). To find the field generated by the superposition of the plates, equation (4.27) can be calculated by using two distances denoted by z_{0i}, where index i = 1, 2 is assigned to the lower and upper plates, respectively. The total field is then found by superposing equation (4.27) as

$$B_{zi}^0(x, y) = B_{z1}^0(x, y) - B_{z2}^0(x, y). \tag{4.28}$$

The numerical approximation for the applied magnetic field described by equation (4.28), is able to replicate a localized field, that is, a magnetic field with high intensity close to the center of the magnet and a fast decay as the distance increases outwards from the center. This approximation allows to consider a magnetic field whose only

contribution points normal to the velocity field and has shown reasonable results as will be seen in the following chapter.

Figure 4.2 shows the magnetic field generated by two magnetized plates of dimensionless units $a = 0.5$ and $b = 0.5$ that were used to replicate a single magnet at the origin of the system. The vertical component of the field is prominent at the center of the plates and its intensity decreases outwards very quickly, thus its contribution at points far from the origin is very small.
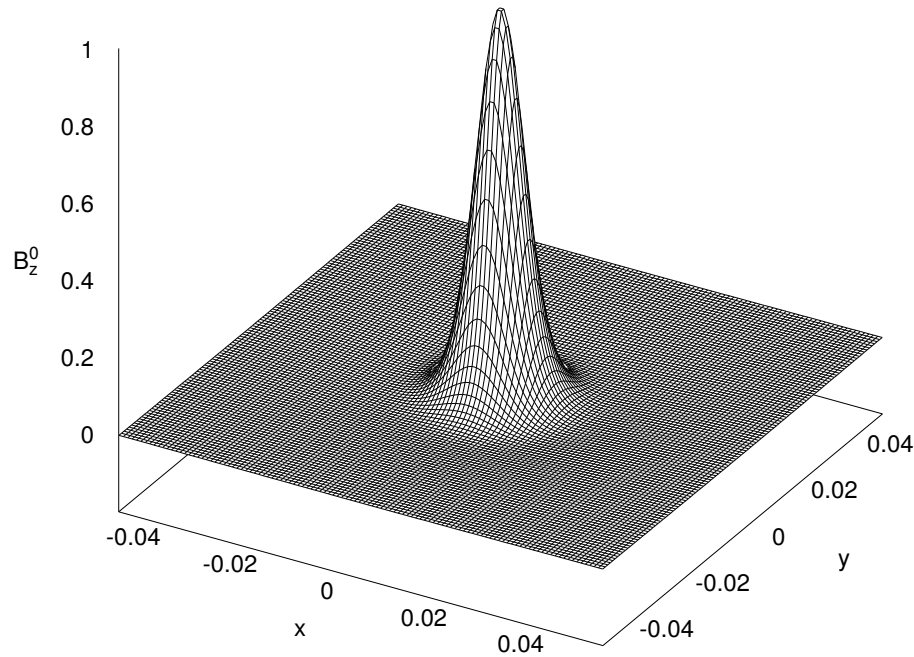

FIGURE 4.2: Applied magnetic field produced by two magnetized square surfaces.

4.2.2 Boundary conditions and initial conditions

Even though the experiment was realized on a cell of rectangular characteristics, for the sake of simplicity, the simulation was tailored to assume a square domain. As will be seen, this approach proved reasonable and good comparisons were achieved. This selection was originated from the small size of the magnet and the large distance of the plexiglass walls to the region of more intense flow. Hence, the flow was simulated on a square domain, and the no–slip condition was imposed at the four boundaries that confined the electrolyte, that is,

$$u = 0,$$
$$v = 0.$$

u = 0
v = 0   S

u = 0   u = 0
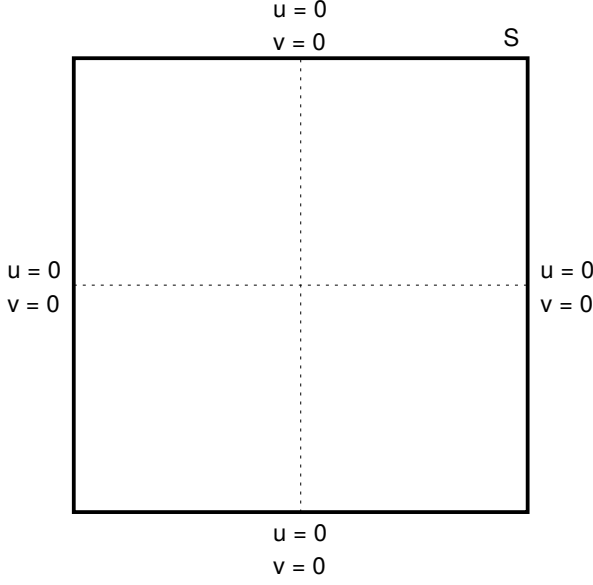v = 0   v = 0

u = 0
v = 0

FIGURE 4.3: Numerical surface.

Figure 4.3 illustrates the domain, where S represents the surface bounding the domain of integration.

The initial conditions were selected as follows:

$$\left.\begin{array}{l} u \quad = 0 \\ v \quad = 0 \end{array}\right\} \quad \text{for all} \quad t = 0,$$

meaning that the fluid is initially at rest.

The conditions on the four walls of figure 4.3 are commonly known as Dirichlet boundary conditions or first–type boundary conditions.

4.2.3 Numerical method

The numerical procedure was based on the finite difference method described by Griebel *et al.* (1998). The procedure was extended to simulate MHD flows by taking into account the Lorentz force (Cuevas *et al.* 2006b). Second order finite difference discretizations were applied on the spatial terms of equations (2.14), (2.15) and (2.16). On the other hand, the temporal terms were discretized using first order Euler's method. The procedure consisted of a structured grid where the velocity components u and v were solved at the horizontal and vertical intersecting points of the grid respectively, while the pressure was solved at the center of the cells. The discretization of the diffusive terms was based on central differences, whereas the convective terms were discretized using a mixture of central differences and a donor–cell method (see Griebel *et al.* (1998, pp. 24–29)).

Time discretizations of $\partial u / \partial t$ and $\partial v / \partial t$ using Euler's method are implemented as

$$\left[\frac{\partial u}{\partial t}\right]^{(n+1)} = \frac{u^{(n+1)} - u^{(n)}}{\Delta t}, \quad \left[\frac{\partial v}{\partial t}\right]^{(n+1)} = \frac{v^{(n+1)} - v^{(n)}}{\Delta t}, \tag{4.29}$$

where superscript (n) represents the derivative at a point n in time t.

The discretization of equations (2.15) and (2.16) then follows

$$u^{(n+1)} = u^{(n)} + \Delta t \left[\left(\frac{\partial^2 u}{\partial x^2} + \frac{\partial^2 u}{\partial y^2}\right) - \frac{\partial (u^2)}{\partial x} - \frac{\partial (uv)}{\partial y} - \frac{\partial P}{\partial x}\right],$$

$$v^{(n+1)} = v^{(n)} + \Delta t \left[\left(\frac{\partial^2 v}{\partial x^2} + \frac{\partial^2 v}{\partial y^2}\right) - \frac{\partial (uv)}{\partial x} - \frac{\partial (v^2)}{\partial y} - Re\, j_x^0 B_z^0 - \frac{\partial P}{\partial y}\right], \tag{4.30}$$

where all values at a point n in time t are known and are referred to as explicit, whereas all values at a time $(n+1)$ still have to be determined and are referred to as implicit.

By denoting

$$F^{(n)} = u^{(n)} + \Delta t \left[\left(\frac{\partial^2 u}{\partial x^2} + \frac{\partial^2 u}{\partial y^2}\right) - \frac{\partial (u^2)}{\partial x} - \frac{\partial (uv)}{\partial y}\right],$$

$$G^{(n)} = v^{(n)} + \Delta t \left[\left(\frac{\partial^2 v}{\partial x^2} + \frac{\partial^2 v}{\partial y^2}\right) - \frac{\partial (uv)}{\partial x} - \frac{\partial (v^2)}{\partial y} - Re\, j_x^0 B_z^0\right], \tag{4.31}$$

equation (4.31) can be expressed as

$$u^{(n+1)} = F^{(n)} - \Delta t \frac{\partial P^{(n+1)}}{\partial x}, \quad \text{and} \quad v^{(n+1)} = G^{(n)} - \Delta t \frac{\partial P^{(n+1)}}{\partial y}. \tag{4.32}$$

The numerical implementation considered that the value of the applied current was $j_x^0 = 1$ in dimensionless terms.

Using this discretization allows to compute the velocity field at time step $(n + 1)$ once the pressure field has been solved. Substituting equation (4.32) in the continuity equation (2.10) results in a Poisson equation for the pressure

$$\frac{\partial^2 P^{(n+1)}}{\partial x^2} + \frac{\partial^2 P^{(n+1)}}{\partial y^2} = \frac{1}{\Delta t} \left(\frac{\partial F^{(n)}}{\partial x} + \frac{\partial G^{(n)}}{\partial y} \right), \tag{4.33}$$

where the pressure corresponds to a time step $(n + 1)$. Note that equation (4.33) requires boundary conditions to be solved.

The pseudo–code to implement the numerical procedure consists of the following:

Algorithm 1 Discretized Navier–Stokes procedure

1: Declare variables and values: $Re, nx, ny...$
2: Compute magnetic field $B_z^0(x, y)$ from Eq.(4.28)
3: $n \leftarrow 0$
4: $u^{(n)} \leftarrow 0, v^{(n)} \leftarrow 0$ and $P^{(n)} \leftarrow 0$
5: **for** $t \leftarrow 1$ to t_{max} **do**
6:     Declare boundary conditions from Fig. (4.3)
7:     Compute $F^{(n)}$ and $G^{(n)}$ from Eq. (4.31)
8:     Compute $P^{(n+1)}$ from Eq. (4.33)
9:     Obtain new velocity field $u^{(n+1)}$ and $v^{(n+1)}$ using Eq. (4.32)
10:     $n \leftarrow n + 1$
11: **end for**

4.2.4 Parameters of the grid, time step and procedure

The numerical solution was simulated inside a dimensionless domain of 30×30. The origin of the magnetic field was axially aligned with the origin of the domain. This was the same case for the superposition of the magnets, the shape was distributed around the origin for a symmetric arrangement, and then aligned with the center of the domain. Using this setup was helpful to simulate a decaying magnetic field from the center outwards. The resolution of the grid was selected at 210×210 in x and y respectively and the time step was given by $\Delta t = 2 \times 10^{-5}$. With these characteristics, the algorithm successfully represented a steady state flow.

Chapter 5

Results

The results of the experimental methodology are shown in this chapter. The experimental velocity fields and streamlines are the result of the PIV analyses and the long exposure photographs, respectively. The numerical and analytical results are qualitatively compared to the experimental results in order to determine if the numerical method and the analytical solution can describe the flow with a good approximation. The results in this section will help to improve the assumptions of the algorithm and the mathematical modeling for a more detailed and accurate description of the experiment.

5.1   Center–magnet arrangement

The results for the center–magnet arrangement are shown in figure 5.1. Particle tracers were added before filming to a considerable uniform density. The main IA was 86 px × 43 px with a 50% offset, and three subsequent IAs were proportional to a 20 px decrease from the previous one (this IA setting was used on all experiments). The velocity field was ultimately obtained from a square ROI of 850 px × 850 px. The PIV software was capable of detecting velocities in the order of 1×10^{-11} m/s, but these values were ignored for practical purposes. From these parameters it was estimated that 1 px $\approx$ 1×10^{-5} mm, so a dimensional visualization region of 3.4 mm × 3.4 mm was obtained.

In figure 5.1(a), two vortices span symmetrically to each side from the center of the magnet. The footprints of the magnets are true in dimension and position in the experimental results which correspond to (a) and (b) in all figures, where blue and red indicate positive and negative polarization, respectively. In the remaining figures, only the origin of the magnetic field is indicated. The left and right vortices rotate counterclockwise and clockwise, respectively. The highest velocity is located on positive y, but remains concentrated inside the diameter of the magnet. The upward displacement of the vortices obeys the direction of the Lorentz force. It is noticed that the displacement is small, which is indicative of the proportional magnitude of the Lorentz force. Nevertheless, the very small displacement of the vortex cores, on the order of $\sim$ 0.2 mm, is due to convective effects of the electromagnetic forcing. On the other hand, there is horizontal asymmetry in the alignment of the vortex cores with respect to each other. Recalling that the forcing strength is small, this issue may be attributed to a phenomenon of particle aggregation. The dipolar flow pattern is characteristic of electromagnetic forcing using one magnet and perpendicular current injection. However, when the magnetic field is generated using two or more magnets, the spatial distribution of the magnets will generate more complex flow patterns that will be characterized by the interaction of multiple vortices. Consequently, the asymmetry in the vortex core alignment could not have been the result of magnetic field interactions.

Based on experimental observations, it is arguable that a case of particle aggregation was present in the core region of the right vortex. Particles must fulfill the conditions of being very small, spherical and neutrally buoyant
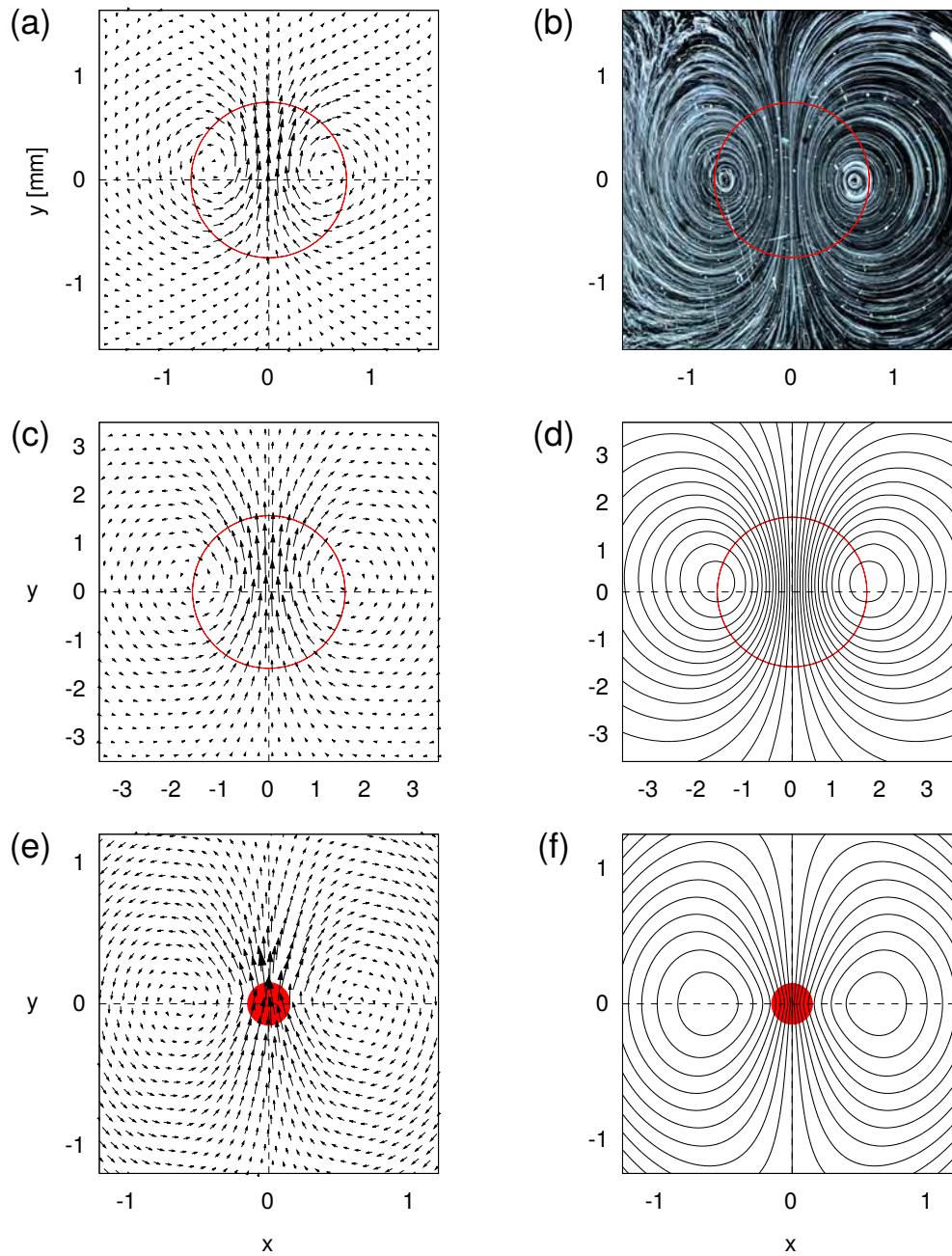
FIGURE 5.1: Center–magnet arrangement. Left column shows velocity fields, right column shows the streamlines. Top row **(a)**, **(b)** experimental results for $Re = 4$. Middle row **(c)**, **(d)** numerical simulation for $Re = 5$. Bottom row **(e)**, **(f)** analytical solution for $Re \approx 0.1$. Axes units for **(a)** and **(b)** correspond to mm. For **(c)**–**(f)**, axes units correspond to dimensionless units.

so they can behave approximately as passive fluid elements. If these conditions are not satisfied, particles will display an inertial behavior relative to the flow by aggregating in regions of high strain, making them take longer

to respond to changes in the flow (Ouellette *et al.* 2008). Once particles aggregate, they form large and heavy structures which are unable to track the flow precisely. If these structures cannot be expelled from the vortex cores, or on the other hand, are expelled and delay incoming particles, then, unsatisfactory samplings will be collected from those sluggish regions. Some techniques, such as two–layer configurations using miscible and immiscible fluids have been used over the years to address the issue of particle clustering (Martell *et al.* 2019; Ouellette *et al.* 2008; Tithof *et al.* 2018). To some extent, the particle aggregation phenomena can be used to justify the misalignment of the vortex cores.

The streamlines shown in figure 5.1(b) are the result of 10 seconds of exposure. Notice how the vortex cores are horizontally aligned with respect to each other. The deformed streamlines close to $x = -1.5$ can be attributed to erratic particles that were unable to follow the flow path faithfully due to particle interactions and effects due to electrolysis (see §5.6) . Unlike the velocimetry results which are averaged, the streamlines correspond to the instantaneous motion of the flow, causing every particle interaction to be reflected in the trajectories of the particles, as can be seen in the exposure. An elliptical deformation of the counter–rotating vortices is clearly appreciated. The deformation is due to the strain field (Huang 2005), which consequently increases the strain inside the vortex structures (Leweke *et al.* 2016). Interesting phenomena can be obtained from these results. Notice for example the white smudge at the top right corner, this is a particle clump being transported very slowly relative to the rest of the particles. Similarly, the right vortex core displays thicker streamlines; presumably, this is also a large particle clump.

Figures 5.1(c) and 5.1(d) are the velocity field and the streamlines of the numerical simulation, respectively. The red circle indicates the position of the magnet but does not physically represent its dimensions. In figure 5.1(c), the highest magnitude of the velocity is well represented since it stays within the diameter of the magnet and follows the direction of the Lorentz force. However, the distance separating the vortex cores is greater than that of the experiment. This can be attributed to the purely 2D approximation where the viscous coupling from the bottom is not taken into account. The displacement of the vortices in the positive y direction represents the effect of the inertial terms, and as is expected, the small displacement is proportional to the magnitude of the Lorentz force. The magnitude of the velocity is also replicated in figure 5.1(d), which can be appreciated from the intensification of the vortex lines close to the origin. Unlike the experiment, the inclination of the vortices is augmented in the simulation, which is better appreciated in the streamlines. Overall, the elliptical shape of the streamlines indicates that the height to width ratio of the vortices is in agreement with the experiment.

Figures 5.1(e) and 5.1(f), are the velocity field and streamlines of the analytical solution for a single magnet, respectively. In both cases, the red circle indicates where the point dipole is located. The highest velocity is exactly on the origin, which coincides with the point of maximum magnetic field intensity. The direction of the velocity obeys the direction of the Lorentz force. Due to the analytical expression, it is visible that the velocity is infinite on the origin of the dipole. This is noticed from figure 5.1(e), at $x = 0$ and $y = 0$ where vectors have an unusually high value due to the indeterminacy. The result is symmetric in figure 5.1(f) with respect to both axes. Such symmetry indicates that the diffusive terms dominate since for this solution convective effects are neglected.

In summary, the elongation of the vortices is aligned with the direction of the force, which in turn drags the recirculation structures in the same direction. Overall, figure 5.1 can be considered as showing great similarity in all the results in terms of a qualitative description.

5.2 Square–magnet arrangement

Electromagnetic forcing to generate vorticity in shallow layers of electrolyte with magnets distributed on the vertices of a square has been previously performed numerically and experimentally. Figueroa (2010) created the magnetic field inside a region of 12 cm × 12 cm, by placing two positively polarized magnets in the top corners

and two negatively polarized magnets in the bottom corners of a 4 cm × 4 cm square. An AC current was applied with multiple forcing frequencies. This configuration, in contrast with figure 5.2(a), resulted in a symmetrical flow pattern characterized by eight vortices and one additional hyperbolic point at the origin. The eight vortices were the result of having magnet pairs of same polarity, which impeded the vortices in between each magnet pair to merge. Similarly, the third hyperbolic point at the origin was caused by the multiple jet collisions. Mixing properties of the quadrilateral magnet arrangement were also determined experimentally and numerically by Figueroa (2010) for the same setup.

In turn, Lara (2013) reported a magnetic field distribution identical to that of figure 5.2(a). The experiment consisted of a 28 cm × 36 cm × 1.3 cm box, with a maximum electrolyte layer height of 0.4 cm. The magnets were distributed inside a square circumscribed in a circle of 8.5 cm diameter, and the forcing was generated with 10 mA of DC current. Analytical streamlines were compared to experimental streamlines observed with colored water (food dye). The analytical solution resulted in symmetrical streamlines similar to those in figure 5.2(f), however, owing to the intensity of the current, the experimental streamlines were not symmetric with respect to the vertical axis. Moreover, it is valuable to mention that DC current was used with intensities ranging from 3 mA to 10 mA for the study of time–independent flows, and 50 mA to 200 mA which resulted in time–dependent flows. In the case of the present work, the applied current is estimated to be 1 mA, which is under the lower threshold for time–independent flows.

In what follows, our results for the square–magnet arrangement are shown in figure 5.2. The particle density was uniform throughout the electrolyte layer before applying the current. The flow pattern was analyzed in a dimensional visualization region of 12 mm × 10 mm. Four magnets of alternate polarity were used, vertically and horizontally spaced by 4 mm, which are shown in figure 5.2(a) and have been labeled from A to D in each quadrant. Since the cell was assembled manually, the magnets were misaligned with respect to each other and did not form a perfect square. From figure 5.2(c), it can be seen that the flow is symmetric with respect to x and y, which is not the case for figure 5.2(a) due to the misalignment of the magnets. The misalignment offset the magnets from the vertices of the square by a factor of approximately 0.5 mm, so to devise the effect of the misalignment on the flow, the circumferences of $ABCD$ have been drawn at a 1:1 scale over the position of the real magnets.

Figures 5.2(a) and 5.2(b) show the experimental velocity field and streamlines, respectively. In figure 5.2(a), it is due to the opposite polarization of the magnet pairs that the co–rotating vortices inside AB and CD merge at startup to form a single vortex of larger magnitude. Therefore, it is visible that the flow is characterized by six vortices. The vortex merging mechanism has been studied extensively (Brandt & Nomura 2006; Cerretelli & Williamson 2003; Huang 2005) and a simplified explanation is convenient. Assuming that two vortices rotate in the same direction a distance from each other, the cores of the vortices will grow to a certain distance a, and the distance separating the cores will reach a value b. When the ratio (a/b) reaches a critical value $(a/b)_c$ the co–rotating vortices will merge and form a single vortex core of superior magnitude than those in isolated rotation.

In a strict sense, the experimental configuration generates a symmetrical flow with respect to both axes. However, owing to the misalignment of the magnets, the flow looses symmetry with respect to $x = 0$ in the top quadrants. Non–linear effects can be appreciated from the displacement of the cores of the main vortices in the direction of the Lorentz force. High velocities concentrate over the magnets and in the region where the main counter–rotating vortices meet.

The streamlines in figure 5.2(b) display an overall symmetry with respect to both axes. However, the outer vortices remain aligned with the magnets, unlike the cores of the main vortices which are displaced toward the direction of the Lorentz force. The flow pattern shows six elliptic points in total which are embedded in each vortex, and two saddle points where the jets converge.
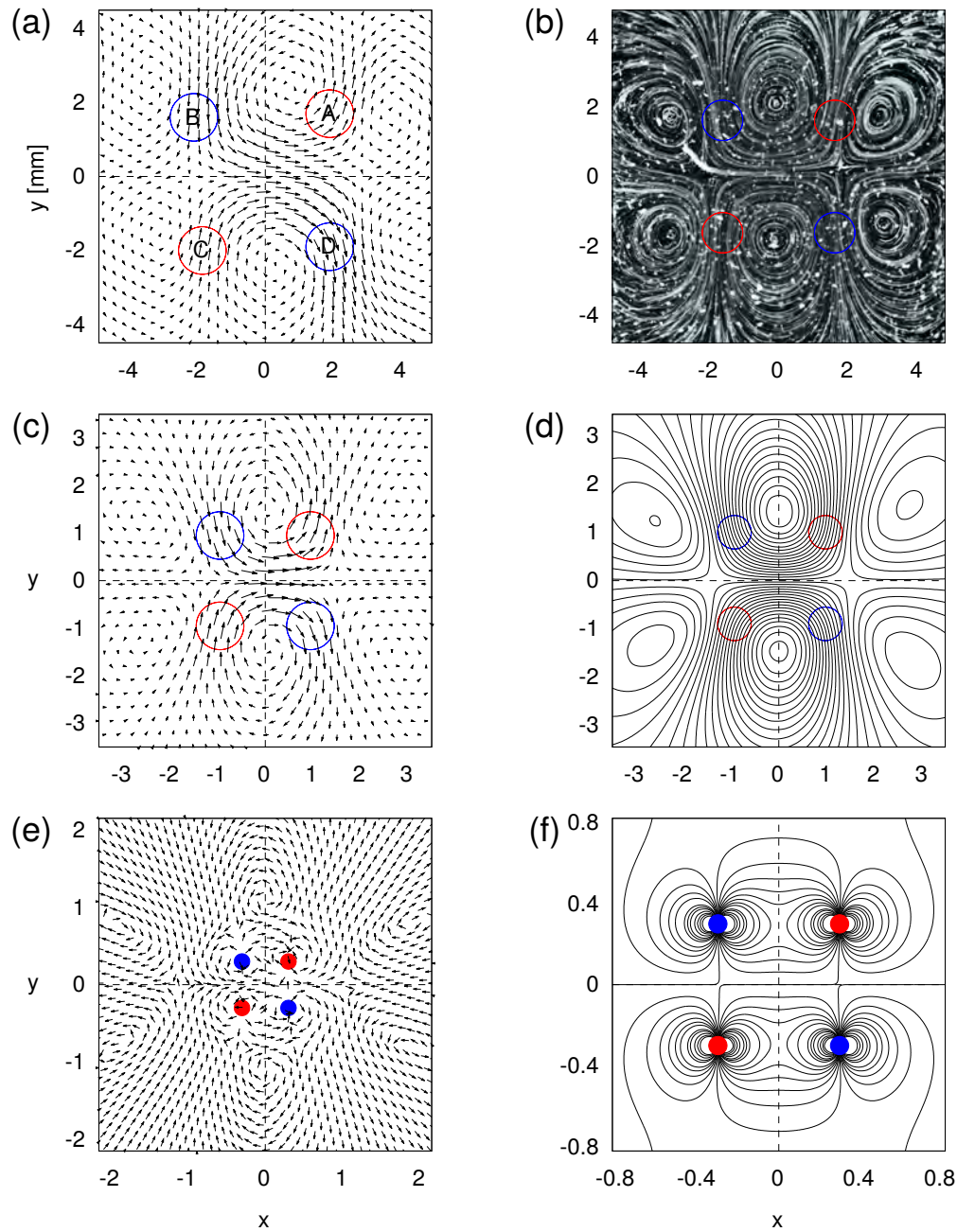
FIGURE 5.2: Square–magnet arrangement. Left column shows velocity fields, right column shows the streamlines. Top row **(a)**, **(b)** experimental results for $Re = 4$. Middle row **(c)**, **(d)** numerical simulation for $Re = 5$. Bottom row **(e)**, **(f)** analytical solution for $Re \approx 0.1$. Axes units for **(a)** and **(b)** correspond to mm. For **(c)**–**(f)**, axes units correspond to dimensionless units.

Figures 5.2(c) and 5.2(d) show the numerical velocity field and streamlines, respectively. A notable feature

in figure 5.2(c) is the somewhat coordinated displacement of all the vortices in the direction of the Lorentz force. Notice, however, an apparent tilting of the main vortical structures which could be attributed to the opposite directions of the Lorentz force in each of the magnets, and to the 2D approximation that does not consider the friction from the bottom wall. The symmetry of the flow pattern can be observed, and the magnitude of the velocity is in agreement with the experimental observation, especially the patch of highest velocity in the central region.

The streamlines in figure 5.2(d) replicate the experimental result very closely. The numerical simulation for the same configuration from Lara (2013), shows that the cores of the main vortices are actually composed of two vortices joined by the outer streamlines, which is due to the separation of the magnets. In our case, the main vortices only show a single core whose vortex lines intensify over the magnets and in the central region of the square. Additionally, the off–center position of the vortex cores shows a great comparison with the experimental result.

Figures 5.2(e) and 5.2(f) show the velocity field and streamlines of the analytical solution, respectively. It is important to recall that a cylindrical magnet was used in the experiments, magnetized square plates were replicated in the numerical simulations, and a point dipole was modeled with a Dirac delta function for the analytical solution. This means that for the analytical solution, the effect of the magnetic field will only be significant at the origin. Consequently, the flow field will be characterized by the multiple vortex interactions, but to a great extent, the point dipole will limit the formation of the intricate flow patterns previously described by the numerical and experimental results.

The vectors have been normalized in figure 5.2(e) (as well as in all results where two or more point dipoles were used) to account for the singularity and avoid erroneous values. The main elements of the flow field are clearly defined, specifically the two main vortices, the four outer vortices, and the direction of the vectors. The streamlines in figure 5.2(f) show that the main vortices are composed of two vortices which cannot merge completely. This describes the effect of the point dipole much better.

In summary, figure 5.2 shows great similarity in the experimental and numerical results in terms of a qualitative description. On the other hand, the analytical solution shows that the point dipole approximation has certain limitations, where the main one lies in accurately replicating vortex interactions. It is, however, precise in capturing the hyperbolic and elliptic points, which are the descriptive properties appreciated in the experimental and numerical results.

5.3 Hexagon–magnet arrangement

Figure 5.3 shows the result for the hexagon–magnet arrangement. Figure 5.3(a) corresponds to the experimental velocity field, where six magnets of alternate polarity were arranged geometrically into a hexagon, and the flow pattern was analyzed in a dimensional visualization region of 11 mm × 11 mm. The flow is characterized by two main vortices rotating in the same direction between AB and DE. Due to the short distance between the magnets, these two vortices are well defined and have the highest velocity, whereas the remaining flow field is determined by low velocity vortices. Owing to the distribution of the magnetic field, the flow pattern should be symmetric with respect to both axes. However, it can be seen that the misalignment of the magnets creates asymmetry mainly with respect to the vertical axis.

The streamlines in figure 5.3(b) reveal that the vortex interactions create complicated flow patters and the merging mechanism cannot be easily predicted due to the intricate distribution of the magnetic field. In turn, the flow is now characterized by the main vortices on top and bottom, and the two auricle shaped figures on left and right with three vortices embedded inside them.
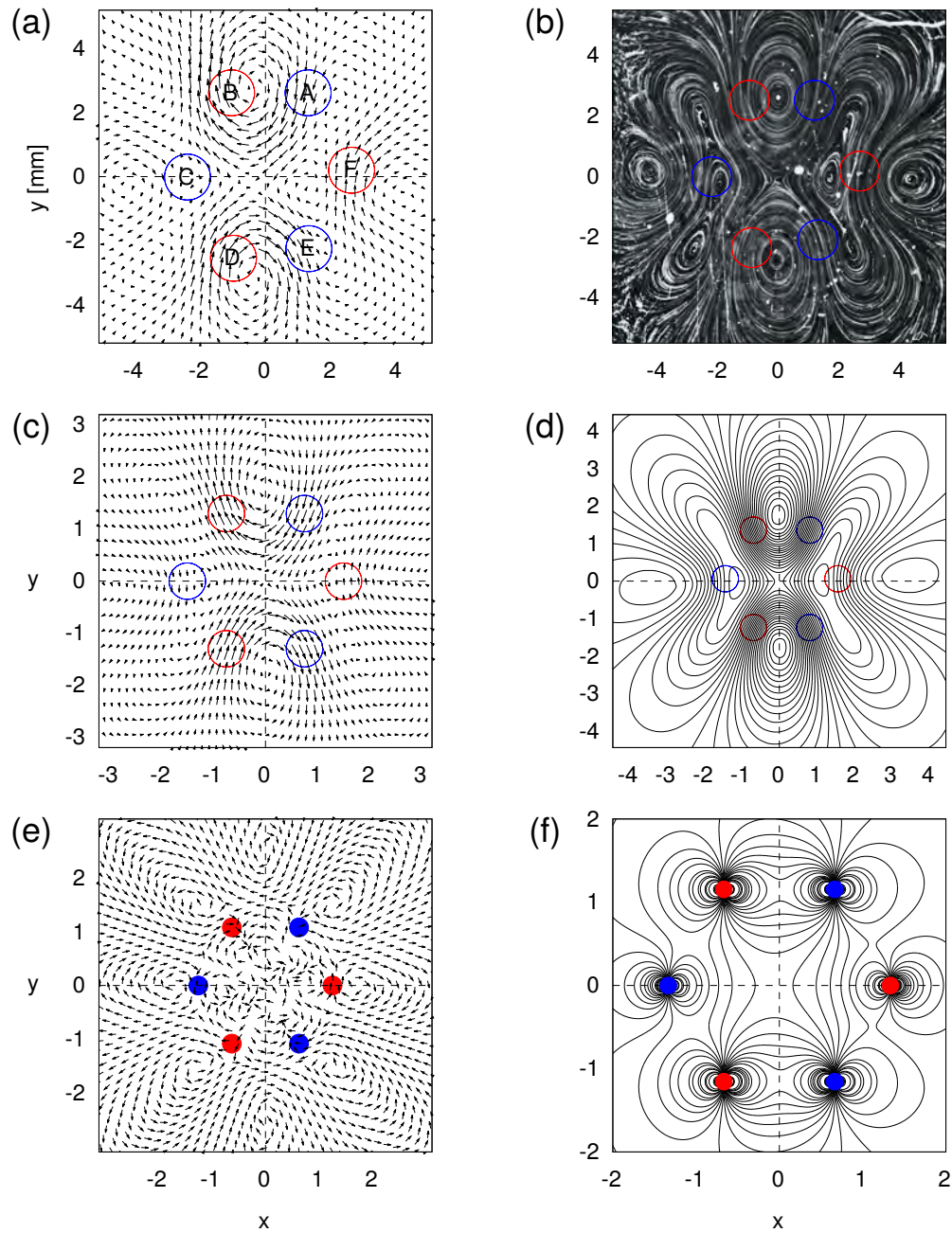
FIGURE 5.3: Hexagon–magnet arrangement. Left column shows velocity fields, right column shows the streamlines. Top row **(a)**, **(b)** experimental results for $Re = 4$. Middle row **(c)**, **(d)** numerical simulation for $Re = 5$. Bottom row **(e)**, **(f)** analytical solution for $Re \approx 0.1$. Axes units for **(a)** and **(b)** correspond to mm. For **(c)**–**(f)**, axes units correspond to dimensionless units.

Figures 5.3(c) and 5.3(d) show the numerical velocity field and streamlines, respectively. In figure 5.3(c), the vectors obey the direction of the Lorentz force, and the main vortex cores are displaced outwards from the center.

In figure 5.3(d), the streamlines intensify over the magnets and a hyperbolic point is clearly defined in the origin. In contrast with figure 5.3(b), the numerical simulation shows that the vortices on left and right are horizontally elongated, which can be attributed to the strict 2D model that does not consider the friction produced by the bottom wall.

Figures 5.3(e) and 5.3(f) show the result of the analytical solution for the velocity field and streamlines, respectively. In comparison with the previous results, figure 5.3(d) does not accurately replicate the flow pattern. However, outside of the hexagon it does replicate the direction of the vectors and the general description of their position with respect to the origin of the magnetic field. Inside the hexagon, the flow field looses symmetry owing to the difficulty of the solution in replicating vortex interactions.

The streamlines in figure 5.3(f) resemble the experimental and numerical results in general, but the comparison is merely descriptive because the characteristic patterns are not completely defined. However, it provides a rough description of how multiple elements are connected throughout the flow field.

In summary, figure 5.3 provides insight into interesting stirring patterns. The experimental and numerical results show great resemblance and useful information can be extracted from the observed phenomena. To some extent, the velocity field of the analytical solution, being merely descriptive, manages to replicate vortex mergers thus providing a good initial approximation to comprehend the actual flow field.

5.4 Checkerboard–magnet arrangement

Figure 5.4 shows the result for the checkerboard–magnet arrangement. Twelve magnets of alternate polarity were distributed on a rectangular lattice with 3 mm of vertical and horizontal spacing between them. A dimensional visualization region of 14×10 mm was ultimately obtained. Figures 5.4(a) and 5.4(b) show the experimental velocity field and streamlines, respectively. A lot of symmetry is observed in figure 5.4(a) with respect to both axes, where multiple vortices and stagnation points are clearly defined. It is arguable that the confinement of the cell and the lattice configuration promotes symmetry in the flow, making the effect of the magnet misalignment be irrelevant to some extent. On the other hand, the misalignment has effect on the velocity distribution, as will be seen later. The streamlines shown in figure 5.4(b) demonstrate the symmetry generated by the lattice and the confinement. This effect can be observed by the well defined elliptic and hyperbolic points. The deformed streamlines on top and bottom are due to the closeness of the magnets with the border of the cell and effects due to electrolysis from the electrodes. The magnetic distribution in this case allows for simpler vortex interactions which leads to predictable flow patterns.

Figures 5.4(c) and 5.4(d) show the numerical velocity field and streamlines, respectively. The result in figure 5.4(c) differs with the experimental field mainly in the distribution of the main vortices, which may be the result of the confinement. However, the rotation of the vortices and the direction of the vectors are in agreement with the Lorentz force. In fact, the highest velocities are located above the magnets. The streamlines in figures 5.4(d) intensify outside of the lattice, which is in fact the opposite effect in comparison with the experimental result. The result is also able to indicate the location of the critical points.

Figures 5.4(e) and 5.4(f) show the analytical solution for the velocity field and streamlines, respectively. The result in figure 5.4(e) shows that most of the flow field cannot be fully described inside the lattice due to the limitations in replicating vortex interactions. Some of the elements in figure 5.4(f) resemble the experimental results closely. For example, the streamlines on the left and right have the same characteristic elongated shape and connect the flow generated by the magnets.

Overall, the results in figure 5.4 help to understand vortex interactions inside a magnetic lattice. The experi-

mental and numerical results closely resemble each other, whereas the analytical solution serves as a decent first approximation.
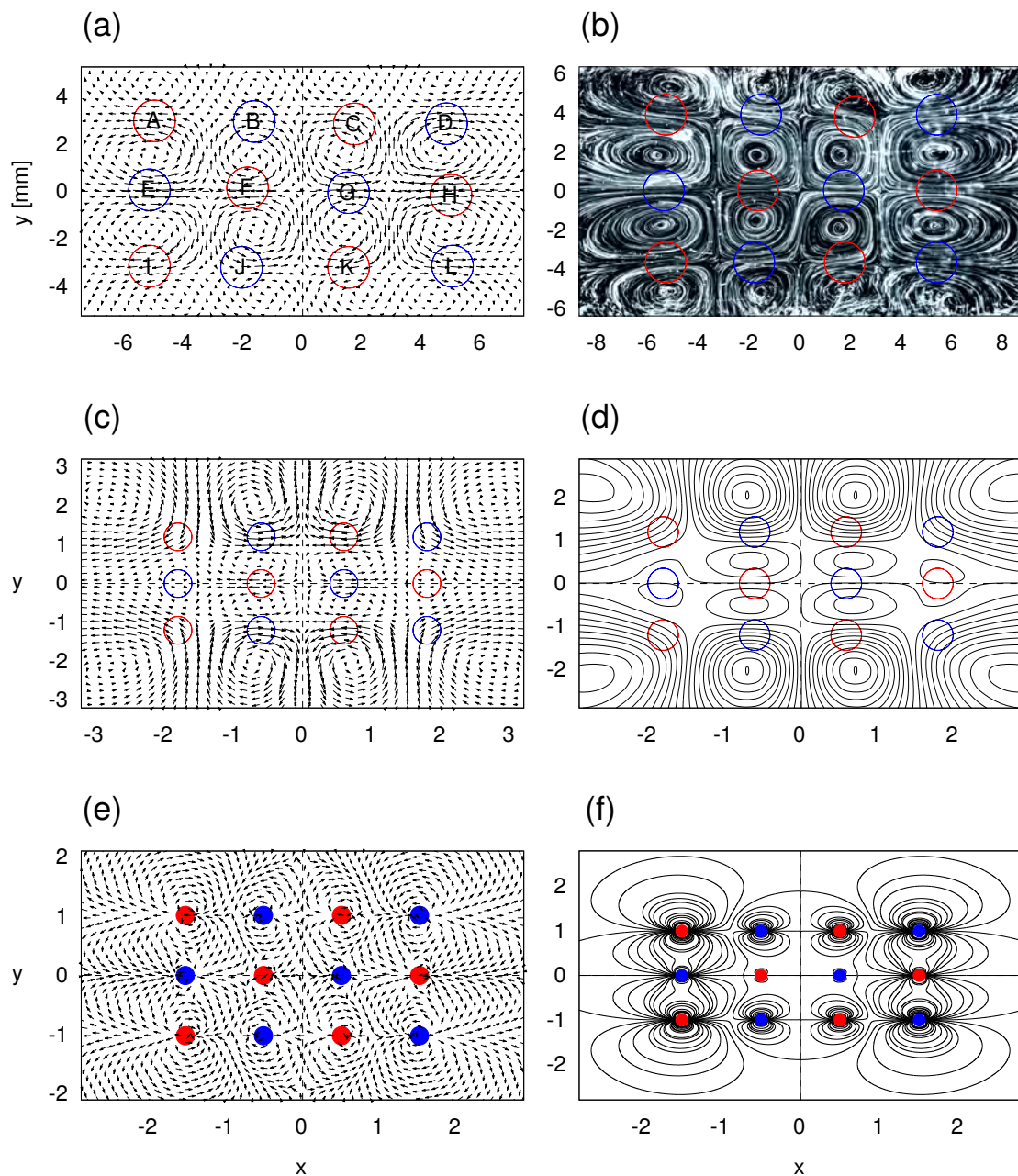

FIGURE 5.4: Checkerboard–magnet arrangement. Left column shows velocity fields, right column shows the streamlines. Top row **(a)**, **(b)** experimental results for *Re* = 4. Middle row **(c)**, **(d)** numerical simulation for *Re* = 5. Bottom row **(e)**, **(f)** analytical solution for *Re* ≈ 0.1. Axes units for **(a)** and **(b)** correspond to mm. For **(c)**–**(f)**, axes units correspond to dimensionless units. Note that the orientation of the figures has been inverted by 90° for presentation purposes.

To summarize, in all the experiments the flow starts by developing a transient regime, then a well-defined vortex pattern is produced, which is determined by the vortex interactions resulting from the distribution of the magnetic field. The resulting flow patterns can be considered symmetric, which is confirmed by the numerical simulations. The asymmetries in the experimental results are caused by physical situations that could not be completely controlled. Three principal situations were electrolytic effects, particle aggregation, and magnet misalignment. The first two introduce errors into the samplings and this is reflected in the resultant velocity fields. The third was due to the manual assembly of the cell.

The flow is mainly defined by diffusive effects, therefore inertial effects can be assumed negligible. Owing to the no-slip condition at the bottom wall, the highest velocities are found at the free surface in a region bounding the diameter of the magnet. Based on experimental observations, the multipolar magnet configurations generated stronger electromagnetic interactions whose strength depends on the distance separating the magnetic poles. The experimental and numerical streamlines were satisfactorily compared, where in all cases, the streamline density intensified as it approached the diameter of the magnet, and reached the highest density over the surface of the magnet.

5.5 Velocity and vorticity maps

The results from the numerical method and the analytical solution were developed in order to have a qualitative point of comparison with the experimental results. However, certain properties of interest such as the velocity magnitude and the vorticity can be extracted from the experimental data. These properties are useful to study the interaction dynamics of the vortices generated by the electromagnetic forcing. In what follows, the velocity and vorticity maps for all the experiments were determined from the experimental data, and are shown in this section.

5.5.1 Velocity maps

As is well known, a velocity map shows the absolute maximums and minimums of the velocity field through the magnitude of the velocity. Such property is a scalar, and can be calculated by taking the square root of the velocity field squared $\sqrt{\vec{u}^2}$, which in the case of a 2D field reduces to $\sqrt{u^2 + v^2}$. The results are useful for the design of particular applications.

In the previous sections, areas of higher intensity were identified based exclusively on observations. From figure 5.5(a), which corresponds to the single–magnet case, it can be observed that the highest velocity, about 1.2 mm/s, is distributed vertically over the center of the magnet. Acceleration regions of proportional value are visible at the entrance and exit of the magnet. These regions at the top and bottom are in accordance with the direction of the Lorentz force. The centers of the vortices can be assumed to posses no velocity at all, whereas the surrounding region has very low velocity, around 0.4 mm/s. A barely distinguishable perimeter of low velocity, about 0.1 mm/s, surrounds the active flow region. This region corresponds to the weak inertial movement of the particles whose energy decreases very quickly in response the viscous flow.

Figure 5.5(b) shows an asymmetric velocity distribution for the square–magnet arrangement, where the highest velocity is dominant over the positively polarized magnets. However, the velocity is vertically elongated in all four magnets, which corresponds to the direction of the Lorentz force. The patch of high velocity in the center of the square corresponds to the place where the counter–rotating vortices meet.

Figure 5.5(c), that corresponds to the hexagon–magnet configuration, shows that the velocity follows the curvature of the vortices and is concentrated on the top and bottom magnet pairs. In fact, the top and bottom pairs are separated by 2 mm, which is the smallest separation distance in all the experiments. The stagnation point in the middle is the meeting point of the co–rotating vortices. In addition, the velocity patches look like pairs of lungs that stem from the center of the hexagon.

Figure 5.5(d) displays a lattice of velocity regions that obey the checkerboard–magnet distribution. The velocity regions at $y = -3, 0, 3$ correspond to horizontal velocity, and it is also where the magnets are placed. The velocity regions at $x = -3, 0, 3$ correspond to vertical velocity. The elongation of the patches is indistinguishable due to the square shape of the figure, however, the horizontal and vertical elongation can be deduced from figure 5.4(a). It is arguable that the lattice configuration homogenizes the velocity distribution, mainly inside the lattice.
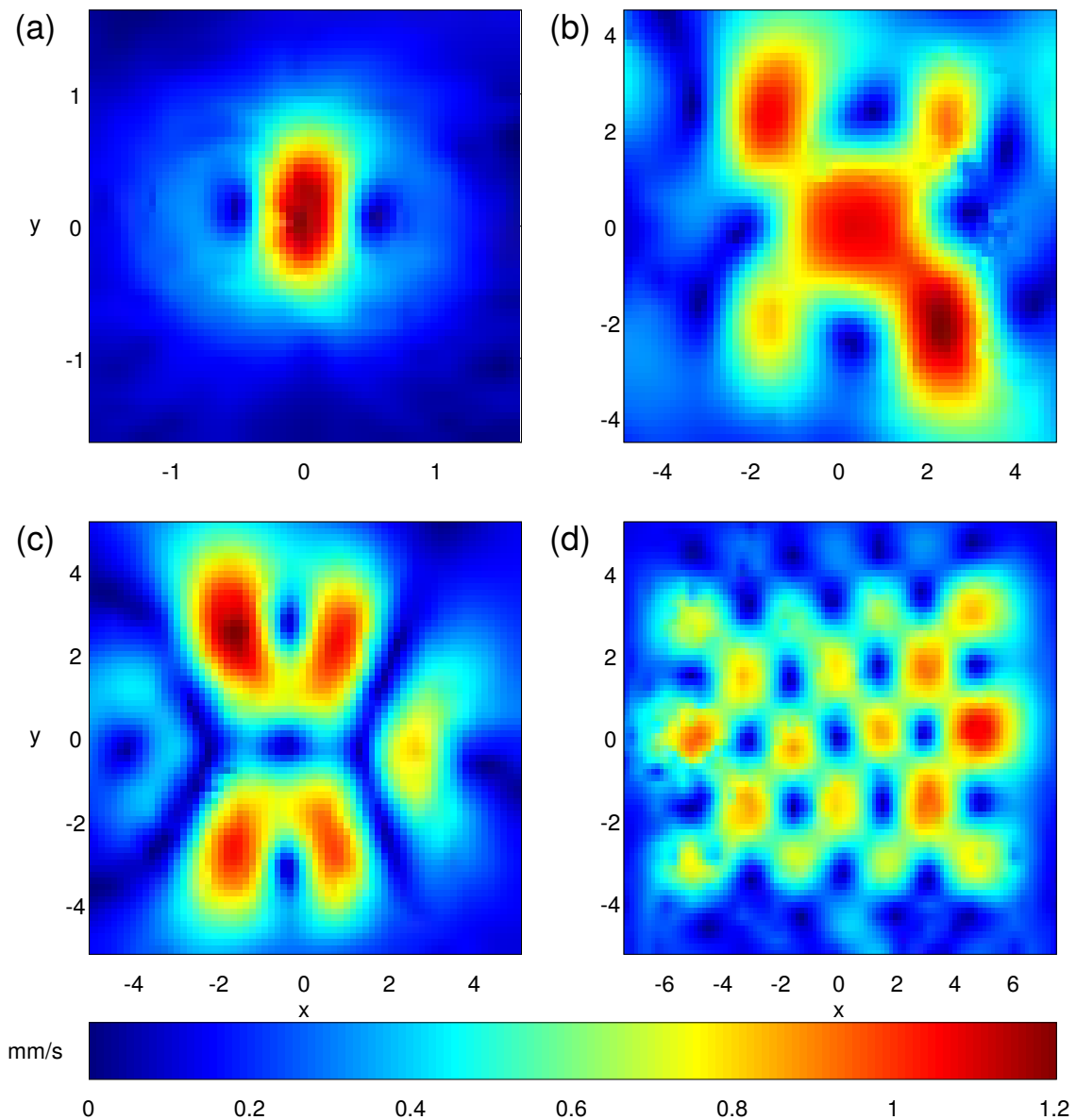

FIGURE 5.5: Experimental velocity maps for the **(a)** center, **(b)** square, **(c)** hexagon, and **(d)** checkerboard–magnet arrangements. Axes units correspond to mm.

5.5.2 Vorticity maps

Figure 5.6 shows the vorticity maps of the explored experimental configurations. It is well known that this property quantifies the local spinning motion of the fluid and is related to the velocity gradients. The highest velocity gradients can be seen in the centers of the vortices where the velocities decrease over very short length scales. The vorticity field can be computed from the experimental information using a discretized vorticity (Griebel *et al.* 1998) making use of the definition

$$\omega_z = \frac{\partial u}{\partial y} - \frac{\partial v}{\partial x},$$

(5.1)

where the derivatives of the velocity with respect to position in equation (5.1) measure the rate of change of velocity. Equation (5.1) is ultimately discretized as

$$\omega_z(i,j) = \frac{u(i,j+1) - u(i,j)}{\Delta y} - \frac{v(i+1,j) - v(i,j)}{\Delta x}.$$

(5.2)

For the case of the experimental vorticity map, Δx and Δy in equation (5.2) correspond to the time step between sequential frames, which is the same time step for the PIV analysis.

From figure 5.6(a) it is clear that the vorticity in the single–magnet case is most intense inside the diameter of the magnet where the velocity gradient is high within a very short distance.

Figure 5.6(b) shows that vorticity in the square–magnet arrangement is overall weak. The strength of the vorticity is almost equal between the merged and single vortices. This can be attributed to the large distance separating the magnets, approximately 4 mm. Additionally, it is noticeable that the merged vortices look like two individual vorticity patches very close to each other. Reducing the distance between the magnets could help in strengthening the interaction force between the magnetic fields while keeping the applied current at a low level.

Intense vorticity can be appreciated in figure 5.6(c) in the main vortices on top and bottom of the hexagonal–magnet arrangement. This is due to the distance separating the magnets (2 mm), which is the shortest distance in all the geometrical shapes, and results in a very strong electromagnetic interaction. The negative vorticity appears to be distributed from top to bottom inside the magnet arrangement. This, however, only corresponds to the resolution of the grid since there are actually three vortices inside each patch. The vortices to the left and right are very weak because the highly viscous nature of the shallow layer quickly dampens the velocity, resulting in a very weak velocity gradient.

Figure 5.6(d) shows a symmetric vorticity distribution in the checkerboard–magnet arrangement with respect to both axes. The highest velocity gradients can be observed inside the lattice which span over very short length scales, on the order of 1 to 1.5 mm, and correspond to the merged vortices. The vorticity is weak outside of the lattice which can be attributed to the effect of viscosity from the low depth of the layer.

Overall, it can be observed that vorticity is higher in regions in between magnets, which can be attributed to a stronger electromagnetic interaction of the electrolyte and the magnetic field produced by a magnet and its neighboring magnet (Pérez-Barrera 2013). This is better observed in figures 5.6(b) and 5.6(c). From a qualitative perspective, the strength of the interaction decreases as the distance increases, and increases as the distance decreases.
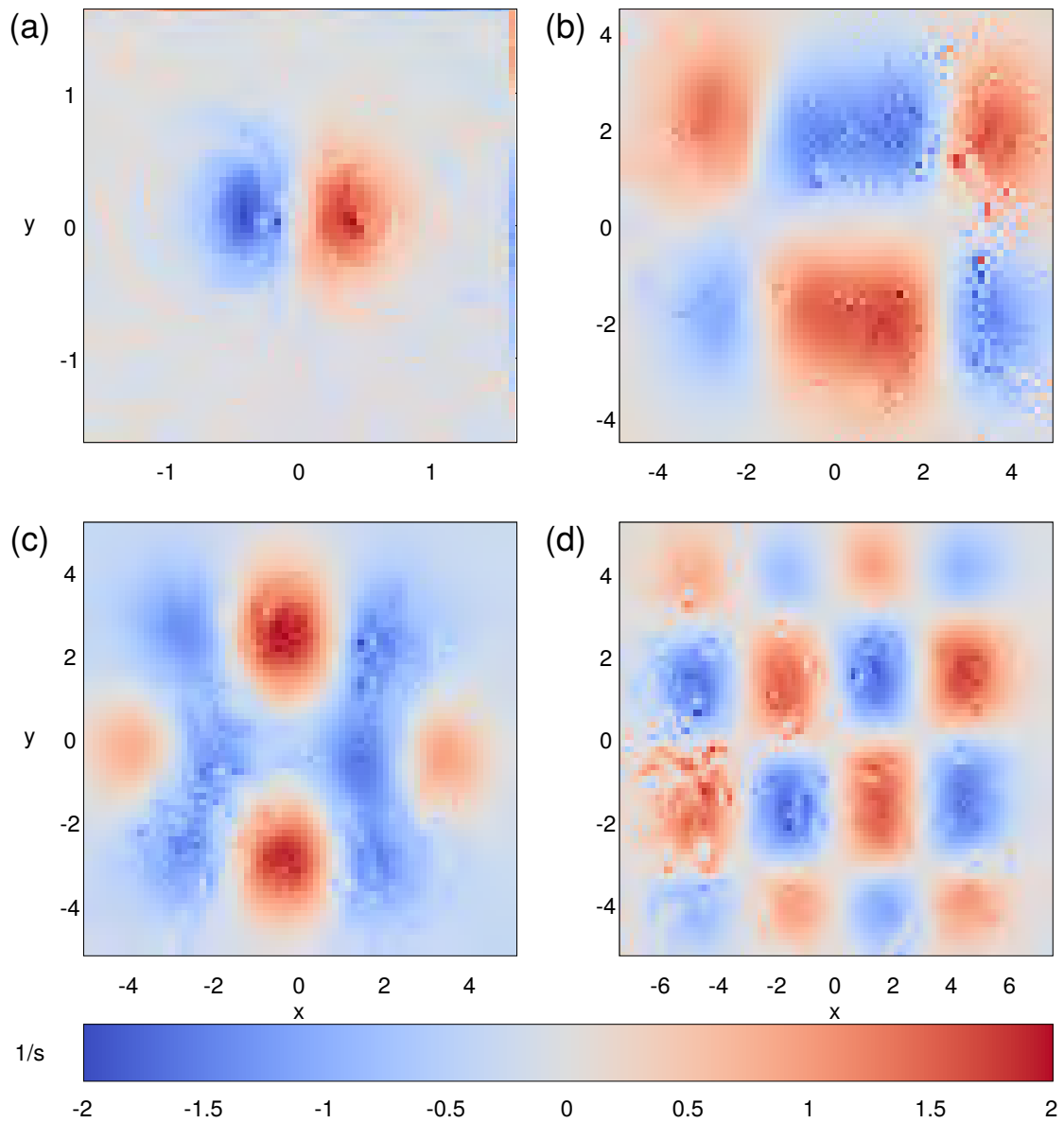
FIGURE 5.6: Experimental vorticity maps for the **(a)** center, **(b)** square, **(c)** hexagon, and **(d)** checkerboard–magnet arrangements. The color bar indicates vorticity ω_z: red corresponds to negative vorticity (clockwise rotation), and blue corresponds to positive vorticity (counterclockwise rotation). Axes units correspond to mm.

5.6 Experimental observations

5.6.1 Particle aggregation

Based on the phenomena observed in figure 5.1(a) where the vortex centroids are offset with respect to each other, some conclusions can be made regarding particle aggregation. Surface tension plays a crucial role in particle aggregation when the particles are at a liquid–gas interface. Surface tension deforms the interface, and the deformation induces a mutual attraction of the floating particles. The multiple interactions eventually motivate the formation of particle clusters (Vella & Mahadevan 2005). The implications of this phenomenon were only captured in the single magnet experiment, however, all experiments were influenced by the deformation of the interface, and many particle clusters were found before and after applying the current.
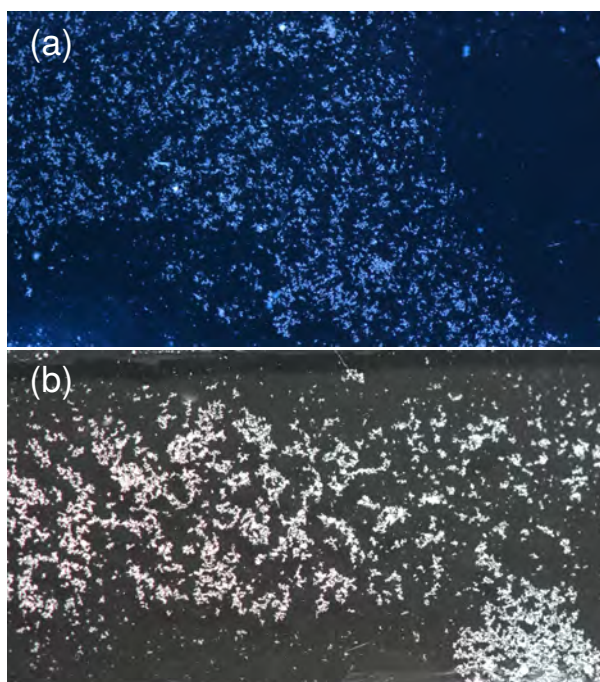

FIGURE 5.7: Particle aggregation patterns after more than one and half minutes of continuous electromagnetic forcing.

One of the main complications owing to this phenomenon is that the particle count is reduced. This effect, along with resistance build up, constrained the footage to 10 seconds of useful material. Nevertheless, the laminar nature of the flow and the very low forcing intensity, allowed to eliminate temporal variations of the flow. In consequence, 10 seconds were satisfactory to confirm that the flow had reached the steady state. A second complication owing to particle aggregation was the slightly less faithful tracking of the flow. To some degree, the particles were larger and some had abandoned regions of the fluid completely (see figure 5.7). The regions without particles were not the main problem because the active flow area remained close to the geometrical center of the cell. However, the larger particles did introduce errors, because these were detected by the PIV software, and in turn, the results yielded many anomalies. This was addressed by constraining the footage to the 10 second period, which was enough time before the problem became significant. Unsatisfactory sampling of sluggish regions owing to particle clusterings has been reported (Kelley & Ouellette 2011; Martell *et al.* 2019).

Lastly, a curious behavior was observed as a consequence of the particle aggregations. Figure 5.7 shows distinctive particle aggregation patterns that were observed after the current was interrupted. Notice the two regions completely void of particles in figure 5.7(a). The blob of particles seems to fill the cell in an otherwise vertical direction, which means that the particles favored an alignment parallel to the direction of the current flow. On the other hand, in figure 5.7(b), a clear strip of particles is formed along the horizontal axis, which is perpendicular to the current flow. It was observed that the effect of electrolysis also contributed to the cluster forming when particle clusters attached to the floating crystals. Over time, this has been avoided by designing electrolyte containers with a trench in the place where the electrodes are positioned. The electrodes are submerged in the trench, which acts like a sewer, and the oxidation byproduct collects in it and prevents it from floating into the electrolyte. Additionally, the use of AC currents has also been reported to prevent electrolytic reactions (Lemoff & Lee 2000). These kind of reactions cause evaporation, bubbling on the electrodes, and in our case, copper oxide, all of which introduce perturbations into the flow.

Certainly, the build up of resistance to current flow heavily influenced the outcome of the experiment. This was due to the DC voltage source that was used. For all the experiments, the source was initialized with a default

value of 5.5 V. Using a multimeter, a reading of ~10 mA was obtained; however, this value decreased very quickly over a very short period. Therefore, the voltage was manually regulated to maintain a somewhat steady current of 1 mA. Nevertheless, fluctuations were inevitable.

5.6.2   Reynolds number

Variations of the Reynolds number affect the flow in several ways. If Re is increased, the effect is interpreted as an intensification of the convective or inertial forces. On the other hand, if Re is decreased, the effect is expressed as an intensification of the diffusive forces. In our case, diffusive forces were dominant. For a determined magnetic field, the value of Re increases as the value of the applied current is increased. In consequence, the Lorentz force intensifies proportionally and generates stronger vorticity. For this work, the Re number was estimated to be 4 in all experiments. In turn, the value of Re for the numerical simulation was 5 to account for fluctuations of the applied current.

However, due to radial decay of the magnetic field, it was observed that inertial effects are more intense in regions where the magnetic field is stronger. This was visible in the displacement of the vortex cores along the direction of the force, which is a non–linear effect and a clear manifestation of the inertial forces.

Chapter 6

Conclusions

We have studied electromagnetically driven vorticity in time–independent flows of shallow electrolyte layers at a millimetric scale through an experimental and theoretical analysis. Direct current was injected perpendicular to the magnetic field created by four geometrical magnet arrangements to generate the Lorentz force, which in turn produced motion in the fluid. The theoretical analysis consisted of an analytical solution and a numerical model. For the experimental analysis, millimetric magnets were used and the flow had place within a 10 mm × 10 mm region.

The analytical solution was obtained using the perturbations method, which allowed to obtain an approximate solution for the low Reynolds number flow. A general solution was obtained for the flow generated by a single magnet, and subsequently this solution was superposed to approximate the flow created by multiple magnets. The assumptions for the boundary conditions were drawn from the experimental parameters. The superposition solution is valid when non–linear effects, manifesting themselves as convective terms, are negligible and the flow is strictly diffusive. Even though a qualitative description is reasonable in terms of an overall description of the flow, several limitations were noticed owing to the use of a magnetic point dipole to model the applied field. Mainly, that the solution struggles to faithfully replicate the interaction of multiple vortices; unlike a single magnet which is otherwise well described. Regardless, the velocity fields and the streamlines obtained with the analytical solution are useful to illustrate and anticipate the behavior of the flow. The limitations motivated a more detailed solution, for which, a numerical simulation was developed.

The numerical method allowed to carry out a more exhaustive analysis. One of the primary features of the numerical method is that the convective terms were fully considered, and that it was designed to replicate a steady state flow. The value of *Re* was 5, which was higher than the experimentally calculated value because, as mentioned, this served as a tolerance that took into account the fluctuation of the electric current. Higher currents can destabilize the flow and lead to a flow whose regime becomes time dependent. Owing to the very small depth of the electrolyte layer, in this first approach the numerical simulation did not consider the effect of the bottom friction. The simulation yielded great results, from which two highlights can be mentioned. The principal is that the displacement of the vortex cores in the direction of the Lorentz force was successfully replicated. The second is that the spatial symmetry of the flows with respect to both axes was well defined. Ultimately, the intensification of the inertial effects on the region where the magnetic is most intense was also well represented. To summarize, the results presented here were in good qualitative agreement with the experiments.

The experimental methodology served as the reference point for all the comparisons. One of the main shortcomings of the cell design was the closeness of the borders to the flow region. In what follows, a second version of the experiment has been designed, which uses a larger cell of square dimensions with electrode trenches and CNC milled holes, so that misalignment errors and electrolytic effects can be minimized. Owing to the small volume of electrolyte, time dependency could not be observed because electrolytic effects appeared very quickly

when high currents were used. Nevertheless, the experimental flows were, to a great extent, stationary, which guarantees that the comparisons coincide satisfactorily with the numerical predictions, at least on a qualitative description.

Much work is left for the future to better characterize the present study. The experimental stage revealed many aspects of the nature of the flow at the millimeter scale that cause great interest. It is urgent to include in the numerical simulation the effect of the bottom friction so that a quantitative comparison can be made. It is also desirable to numerically incorporate elements such as electrochemical effects, changes in temperature and composition of the medium for a more accurate description of the flow. Additionally, a Lagrangian particle tracking analysis could be useful for the prediction of mixing properties. It is well known that the confinement of the flow and the viscous coupling of the bottom dissipate and stabilize the flow, therefore, a study leading to a periodic or a chaotic flow regime could result in intriguing phenomena. It is of particular interest to apply the theory and experiments on a smaller scale that could eventually lead to the study of microfluidic applications.

Bibliography

Akkermans, R. A. D., Cieslik, A. R., Kamp, L. P. J., Trieling, R. R., Clercx, H. J. H., & van Heijst, G. J. F. (2008). The three-dimensional structure of an electromagnetically generated dipolar vortex in a shallow fluid layer. *Physics of Fluids*, *20*(11), https://doi.org/10.1063/1.3005452, 116601. https://doi.org/10.1063/1.3005452

Brandt, L. K., & Nomura, K. K. (2006). The physics of vortex merger: Further insight. *Physics of Fluids*, *18*(5), https://doi.org/10.1063/1.2201474, 051701. https://doi.org/10.1063/1.2201474

Bühler, L. (2007). Liquid metal magnetohydrodynamics for fusion blankets. In *Magnetohydrodynamics: Historical evolution and trends* (pp. 171–194). Dordrecht, Springer Netherlands. https://doi.org/10.1007/978-1-4020-4833-3_10

Cerretelli, C., & Williamson, C. H. K. (2003). The physical mechanism for vortex merging. *Journal of Fluid Mechanics*, *475*, 41–77. https://doi.org/10.1017/S0022112002002847

Cuevas, S., Smolentsev, S., & Abdou, M. (2006a). Vorticity generation in creeping flow past a magnetic obstacle. *Phys. Rev. E*, *74*, 056301. https://doi.org/10.1103/PhysRevE.74.056301

Cuevas, S., Smolentsev, S., & Abdou, M. (2006b). Vorticity generation in localized magnetic fields. *Magnetohydrodynamics*, *42*(2–3), 199–206. https://doi.org/http://doi.org/10.22364/mhd

Davidson, P. A. (2017). *Introduction to magnetohydrodynamics* (2nd ed.). Cambridge, Cambridge University Press. https://doi.org/10.1017/9781316672853

Figueroa, A. (2006). *Generación de vorticidad mediante fuerzas magnéticas* (Master's Thesis). UNAM. Mexico.

Figueroa, A., Cuevas, S., & Ramos, E. (2011). Electromagnetically driven oscillatory shallow layer flow. *Physics of Fluids*, *23*(1), 013601. https://doi.org/10.1063/1.3531729

Figueroa, A. (2010). *Dynamics of electromagnetically driven vortices* (PhD Thesis). UNAM. Mexico.

Figueroa, A., Demiaux, F., Cuevas, S., & Ramos, E. (2009). Electrically driven vortices in a weak dipolar magnetic field in a shallow electrolytic layer. *Journal of Fluid Mechanics*, *641*, 245–261. https://doi.org/10.1017/S0022112009991868

Figueroa, A., Meunier, P., Cuevas, S., Villermaux, E., & Ramos, E. (2014). Chaotic advection at large péclet number: Electromagnetically driven experiments, numerical simulations, and theoretical predictions. *Physics of Fluids*, *26*(1), https://doi.org/10.1063/1.4861004, 013601. https://doi.org/10.1063/1.4861004

Good, R. H., & Nelson, T. J. (1971). *Classical theory of electric and magnetic fields*. Academic Press.

Griebel, M., Dornseifer, T., & Neunhoeffer, T. (1998). *Numerical simulation in fluid dynamics: A practical introduction*. SIAM.

Hahn, D. W., & Özişik, M. N. (2012). *Heat conduction* (3rd ed.). John Wiley & Sons, Inc.

Huang, M.-J. (2005). The physical mechanism of symmetric vortex merger: A new viewpoint. *Physics of Fluids*, *17*(7), https://doi.org/10.1063/1.1949647, 074105. https://doi.org/10.1063/1.1949647

Kelley, D. H., & Ouellette, N. T. (2011). Onset of three-dimensionality in electromagnetically driven thin-layer flows. *Physics of Fluids*, *23*(4), https://doi.org/10.1063/1.3570685, 045103. https://doi.org/10.1063/1.3570685

Khoshmanesh, K., Tang, S.-Y., Zhu, J. Y., Schaefer, S., Mitchell, A., Kalantar-zadeh, K., & Dickey, M. D. (2017). Liquid metal enabled microfluidics. *Lab Chip*, *17*, 974–993. https://doi.org/10.1039/C7LC00046D

Kline, S. (1969). Film notes for flow visualization. *National Committee for Fluid Mechanics Films*, (21607). https://web.mit.edu/hml/ncfmf.html

Lara, C. G. (2013). *Estudio teórico–experimental de la agitación electromagnética de flujos en aguas someras* (Master's Thesis). UNAM. Mexico.

Lemoff, A. V., & Lee, A. P. (2000). An ac magnetohydrodynamic micropump. *Sensors and Actuators B: Chemical*, *63*(3), 178–185. https://doi.org/https://doi.org/10.1016/S0925-4005(00)00355-5

Leweke, T., Le Dizès, S., & Williamson, C. H. (2016). Dynamics and instabilities of vortex pairs. *Annual Review of Fluid Mechanics*, *48*(1), https://doi.org/10.1146/annurev-fluid-122414-034558, 507–541. https://doi.org/10.1146/annurev-fluid-122414-034558

Martell, B. C., Tithof, J., & Kelley, D. H. (2019). Comparing free surface and interface motion in electromagnetically driven thin-layer flows. *Phys. Rev. Fluids*, *4*, 043904. https://doi.org/10.1103/PhysRevFluids.4.043904

McCaig, M. (1977). *Permanent magnets in theory and practice*. Wiley.

Ouellette, N. T., O'Malley, P. J. J., & Gollub, J. P. (2008). Transport of finite-sized particles in chaotic flow. *Phys. Rev. Lett.*, *101*, 174504. https://doi.org/10.1103/PhysRevLett.101.174504

Pérez-Barrera, J. (2013). *Estudio teórico del flujo producido por una fuerza de lorentz azimutal en un agitador electromagnético* (Master's Thesis). UNAM. Mexico.

Qian, S., Zhu, J., & Bau, H. H. (2002). A stirrer for magnetohydrodynamically controlled minute fluidic networks. *Physics of Fluids*, *14*(10), https://doi.org/10.1063/1.1504713, 3584–3592. https://doi.org/10.1063/1.1504713

Rossen, N. S., Tarp, J. M., Mathiesen, J., Jensen, M. H., & Oddershede, L. B. (2014). Long–range ordered vorticity patterns in living tissue induced by cell division. *Nature Communications*, *5*(5720). https://doi.org/10.1038/ncomms6720

Salas, H., Cuevas, S., & Ramos, E. (2001). Electrically driven vortices in a dipolar magnetic field. *Magnetohydrodynamics*, *37*(1-2), 38–44.

Schöll, R., Henke, R., & Neuwerth, G. (2010). Vortex sheets of aircraft in takeoff and landing (W. Schröder, Ed.). In W. Schröder (Ed.), *Summary of flow modulation and fluid-structure interaction findings*, Berlin, Heidelberg, Springer Berlin Heidelberg.

Sommeria, J. (1988). Electrically driven vortices in a strong magnetic field. *Journal of Fluid Mechanics*, *189*, 553–569. https://doi.org/10.1017/S0022112088001144

Stanley, G. T., Rui, C., Guoyi, T., Leidong, M., & Tse, Z. T. H. (2016). The magnetohydrodynamic effect and its associated material designs for biomedical applications: A state-of-the-art review. *Advanced Functional Materials*, *26*(22), 3942–3952. https://doi.org/10.1002/adfm.201504198

Thielicke, W. (2014). *The flapping flight of birds – analysis and application, phd thesis*. Netherlands, Rijksuniversiteit Groningen. http://irs.ub.rug.nl/ppn/382783069

Thielicke, W., & J. Stamhuis, E. J. (2019). Pivlab - time-resolved digital particle image velocimetry tool for matlab (version 2.31), http://PIVlab.blogspot.com. http://www.mathworks.com/matlabcentral/fileexchange/27659-pivlab-time-resolved-particle-image-velocimetry--piv--tool

Thielicke, W., & Stamhuis, E. J. (2014). Pivlab – towards user-friendly, affordable and accurate digital particle image velocimetry in matlab. *Journal of Open Research Software*, *2*(1), https://doi.org/10.1119/1.1898523, e30. https://doi.org/http://doi.org/10.5334/jors.bl

Thompson, J. M. T., & Robb McDonald, N. (1999). The motion of geophysical vortices. *Philosophical Transactions of the Royal Society of London. Series A: Mathematical, Physical and Engineering Sciences*, *357*(1763), https://royalsocietypublishing.org/doi/pdf/10.1098/rsta.1999.0501, 3427–3444. https://doi.org/10.1098/rsta.1999.0501

Tithof, J., Martell, B. C., & Kelley, D. H. (2018). Three-dimensionality of one- and two-layer electromagnetically driven thin-layer flows. *Phys. Rev. Fluids*, *3*, 064602. https://doi.org/10.1103/PhysRevFluids.3.064602

Vella, D., & Mahadevan, L. (2005). The "cheerios effect". *American Journal of Physics*, *73*(9), 817–825. https://doi.org/10.1119/1.1898523

Veronis, G. (1970). The analogy between rotating and stratified fluids. *Annual Review of Fluid Mechanics*, *2*(1), https://doi.org/10.1146/annurev.fl.02.010170.000345, 37–66. https://doi.org/10.1146/annurev.fl.02.010170.000345

Villermaux, E. (2019). Mixing versus stirring. *Annual Review of Fluid Mechanics*, *51*(1), 245–273. https://doi.org/10.1146/annurev-fluid-010518-040306

Westerweel, J., & Scarano, F. (2005). Universal outlier detection for piv data. *Exp Fluids*, *39*, 1096–1100. https://doi.org/https://doi.org/10.1007/s00348-005-0016-6

Yi, M., Qian, S., & Bau, H. H. (2002). A magnetohydrodynamic chaotic stirrer. *Journal of Fluid Mechanics*, *468*, 153–177. https://doi.org/10.1017/S0022112002001635

Appendix A
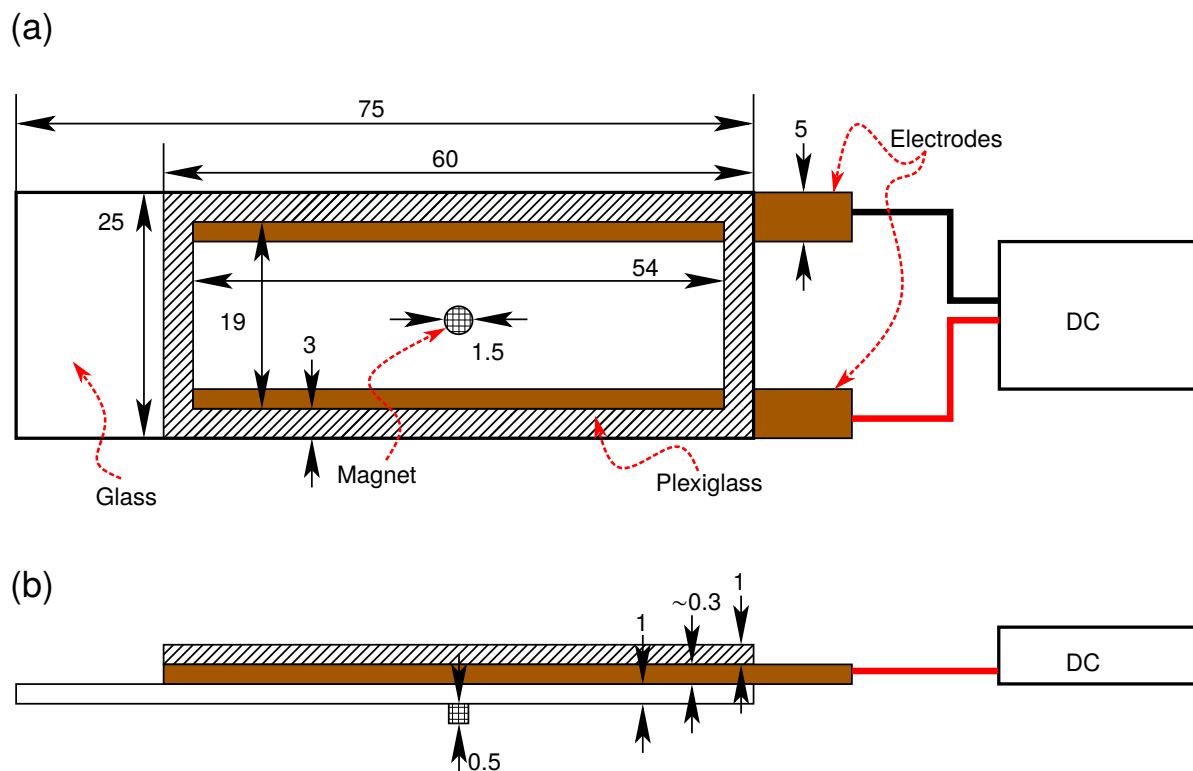
Experimental cell dimensions

(a)

(b)

FIGURE A.1: **(a)** Top view. The components are drawn at a 1:1.3 scale (except for the magnet) for presentation purposes. **(b)** Side view. The width of the components is drawn out of scale to visualize their dimensions and place. Units correspond to mm.